

## WISE J233237.05–505643.5: A DOUBLE-PEAKED, BROAD-LINED ACTIVE GALACTIC NUCLEUS WITH A SPIRAL-SHAPED RADIO MORPHOLOGY

CHAO-WEI TSAI<sup>1,2</sup>, T. H. JARRETT<sup>3</sup>, DANIEL STERN<sup>2</sup>, BJORN EMONTS<sup>4,5</sup>, R. SCOTT BARROWS<sup>6</sup>, ROBERTO J. ASSEF<sup>2,7</sup>, RAY P. NORRIS<sup>5</sup>, PETER R. M. EISENHARDT<sup>2</sup>, CAROL LONSDALE<sup>8</sup>, ANDREW W. BLAIN<sup>9</sup>, DOMINIC J. BENFORD<sup>10</sup>, JINGWEN WU<sup>2</sup>, BRIAN STALDER<sup>11</sup>, CHRISTOPHER W. STUBBS<sup>11</sup>, F. WILLIAM HIGH<sup>12</sup>, K. L. LI<sup>13</sup>, AND ALBERT K. H. KONG<sup>13</sup>

<sup>1</sup> Infrared Processing and Analysis Center, California Institute of Technology, Pasadena, CA 91125, USA

<sup>2</sup> Jet Propulsion Laboratory, California Institute of Technology, 4800 Oak Grove Dr., Pasadena, CA 91109, USA; Chao-Wei.Tsai@jpl.nasa.gov

<sup>3</sup> Astronomy Department, University of Cape Town, Private Bag X3, Rondebosch 7701, South Africa

<sup>4</sup> Centro de Astrobiología (INTA-CSIC), Ctra de Torrejón a Ajalvir, km 4, E-28850 Torrejón de Ardoz, Madrid, Spain

<sup>5</sup> Australia Telescope National Facility, CSIRO Astronomy and Space Science, P.O. Box 76, Epping NSW 1710, Australia

<sup>6</sup> Arkansas Center for Space and Planetary Sciences, University of Arkansas, Fayetteville, AR 72701, USA

<sup>7</sup> Núcleo de Astronomía de la Facultad de Ingeniería, Universidad Diego Portales, Av. Ejército Libertador 441, Santiago, Chile

<sup>8</sup> National Radio Astronomy Observatory, 520 Edgemont Road, Charlottesville, VA 22903, USA

<sup>9</sup> Department of Physics and Astronomy, University of Leicester, I University Road, Leicester LE1 7RH, UK

<sup>10</sup> NASA Goddard Space Flight Center, Greenbelt, MD 20771, USA

<sup>11</sup> Harvard-Smithsonian Center for Astrophysics, 60 Garden Street, Cambridge, MA 02138, USA

<sup>12</sup> Kavli Institute for Cosmological Physics, University of Chicago, 5640 South Ellis Avenue, Chicago, IL 60637, USA

<sup>13</sup> Institute of Astronomy and Department of Physics, National Tsing Hua University, Hsinchu 30013, Taiwan

Received 2012 December 25; accepted 2013 October 5; published 2013 November 25

### ABSTRACT

We present radio continuum mapping, optical imaging, and spectroscopy of the newly discovered double-peaked, broad-lined active galactic nucleus (AGN) WISE J233237.05–505643.5 at redshift  $z = 0.3447$ . This source exhibits an FR-I and FR-II hybrid morphology, characterized by a bright core, jet, and Doppler-boosted lobe structures in Australian Telescope Compact Array continuum maps at 1.5, 5.6, and 9 GHz. Unlike most FR-II objects, W2332–5056 is hosted by a disk-like galaxy. The core has a projected 5'' linear radio feature that is perpendicular to the curved primary jet, hinting at unusual and complex activity within the inner 25 kpc. The multi-epoch, optical-near-IR photometric measurements indicate significant variability over a 3–20 yr baseline from the AGN component. Gemini South optical data show unusual double-peaked emission-line features: the centroids of the broad-lined components of H $\alpha$  and H $\beta$  are blueshifted with respect to the narrow lines and host galaxy by  $\sim 3800 \text{ km s}^{-1}$ . We examine possible cases that involve single or double supermassive black holes in the system and discuss the required future investigations to disentangle the mysterious nature of this system.

**Key words:** galaxies: active – galaxies: individual: WISE J233237.05–505643.5 – galaxies: interactions – galaxies: jets – galaxies: nuclei – radio continuum: galaxies

**Online-only material:** color figures

### 1. INTRODUCTION

The discovery of supermassive black holes (SMBHs) with masses larger than 10 billion solar masses in two nearby galaxies (McConnell et al. 2011, 2012) highlights the need to understand how SMBHs grow and influence galaxy evolution. Two commonly accepted growth processes are accretion from the interstellar medium (ISM) and SMBH mergers (Alexander & Hickox 2012). The latter scenario is thought to play a more dominant role for SMBH growth in the early universe, although binary active galactic nuclei (AGNs) seen at late stages in the merging of bulge-dominated galaxies should still be relatively common in the nearby universe. However, despite significant efforts searching for resolved binary AGNs (e.g., Komossa et al. 2003; Rodriguez et al. 2006; Civano et al. 2010; Green et al. 2010; Fu et al. 2011a, 2012; Comerford et al. 2012; Barrows et al. 2012) and late-stage (unresolved) merging SMBHs (Ju et al. 2013; Shen et al. 2013), such systems appear to be very rare. Two potential signatures of merging SMBHs are from their complicated radio morphology (see Baumgarte & Shapiro 2011) and unusual spectroscopic features such as velocity offsets between broad and narrow spectral line components (see the review by Popović 2012; Komossa 2012).

SMBH binaries are the inevitable result of galaxy formation. In a major galaxy merger event, the SMBHs hosted in two large

merging galaxies dynamically interact as the parent galaxies coalesce and form a final bulge. SMBH merging can be considered in three stages (see Merritt & Milosavljević 2005; Bogdanović et al. 2008 and references therein). In the first stage, the SMBHs dissipate their angular momentum through dynamical friction with surrounding stars, thus reducing their orbits. This process is efficient near the nuclear region of the host galaxy where the stellar density is high, but stalls at radii of  $\sim 0.01$ –10 pc due to the depletion of stars. SMBHs spend the majority of their lifetime at this close separation (Begelman et al. 1980; Yu 2002). However, if the system contains a gaseous accretion disk, the binary orbit could decay further via interaction between the SMBH binary and the gas (Escala et al. 2004, 2005; Dotti et al. 2007, 2009). This is the so-called “intermediate stage,” lasting for a few to a few dozen Myr. In the final stage, when two SMBHs are brought close enough, the binary orbital angular momentum dissipates efficiently via gravitational radiation and the SMBHs proceed to final coalescence.

A multi-jet radio morphology is potentially strong evidence for SMBH binaries or SMBH mergers. In the case of 3C 75 ( $z = 0.0232$ ), four radio jets are launched from a pair of accreting AGNs separated by 8 kpc (Owen et al. 1985; Yokosawa & Inoue 1985). In another case, the radio galaxy 3C 66B ( $z = 0.0215$ ) shows zig-zag patterns of compact radio

jets associated with a SMBH binary, separated by  $4 \times 10^{-3}$  pc in a 1.1 yr orbital period (Sudou et al. 2003). Iguchi et al. (2010) calculated that the decay time of the 3C 66B orbit is about 500 yr due to gravitational radiation, although a pulsar timing experiment did not detect the expected gravitational waves from this binary to a 95% confidence level (Jenet et al. 2004). From their short lifetimes, SMBH binary systems with small orbital separations and short orbital periods are expected to be very rare. X-shaped radio galaxies (XRGs; Leahy & Parma 1992), a subclass of Fanaroff–Riley Class II (FR-II; Fanaroff & Riley 1974) objects, contain two misaligned pairs of centrosymmetric radio lobes originating from an elliptical galaxy host. Usually one pair of more extended lobes with low surface brightness is oriented at a large angle with respect to a pair of less extended, high surface brightness lobes. Their radio morphology has been suggested as a sign of rapidly changing SMBH spin, possibly tracing a SMBH merging event (Dennett-Thorpe et al. 2002; Merritt & Ekers 2002; Gopal-Krishna et al. 2003). Other proposed explanations for XRGs include back-flowing material from jets deflected off the ISM, outflow from over-pressured cocoons, or interactions of jets with stellar and intergalactic shells (Leahy & Williams 1984; Worrall et al. 1995; Capetti et al. 2002; Hedges-Kluck et al. 2010). These models have been tested in X-ray and optical spectroscopic morphological studies (e.g., Saripalli & Subrahmanyam 2009; Cheung et al. 2009; Landt et al. 2010; Hedges-Kluck et al. 2010). A recent review of observational evidence argues that none of the proposed models can explain all of the observed properties of XRGs (Gopal-Krishna et al. 2010).

In optical spectroscopy, host galaxies with broad emission lines significantly Doppler-shifted from the corresponding narrow lines (NLs) have been interpreted as the consequence of a late-stage SMBH merger or, alternatively, due to a kick received by the broad-lined SMBH resulting from anisotropic gravitational emission (González et al. 2007; Civano et al. 2010). Theoretical models predict a maximum “kick” velocity of  $\sim 4000$  km s $^{-1}$  for a merger inspiraling on a quasi-circular orbit (Campanelli et al. 2007). In certain unusual orbit configurations such as hyperbolic encounters, the velocity displacement  $\Delta V$  between NLs and broad lines (BLs) can reach 10,000 km s $^{-1}$  (Healy et al. 2009). Observationally, however, large BL–NL velocity offsets are not commonly seen. In the past few years, studies that mine the Sloan Digital Sky Survey (SDSS) spectroscopic archive have identified only 16 objects whose broad Balmer lines are offset from the NLs by  $>3500$  km s $^{-1}$  (Komossa et al. 2003; Boroson & Lauer 2009; Shields et al. 2009; Steinhardt et al. 2012; Tsalmantza et al. 2011; Eracleous et al. 2012). In addition, two alternate models have also been proposed to explain this unusual spectral configuration in these objects: (1) a line-of-sight superposition of two unrelated AGNs (e.g., Shields et al. 2009) and (2) an asymmetric Keplerian accretion disk (Chen & Halpern 1989).

The accretion disk model, which requires a centrally illuminated, geometrically thin, and optically thick accretion disk, has successfully explained the double-peaked BL emitters (“double-peaked emitters” or DPEs; Bonning et al. 2007; Shields et al. 2009; Eracleous et al. 2009). It is expected that accretion disks should naturally become circular after a period of time (Rees 1988; Cannizzo et al. 1990) and for this reason the circular, Keplerian disk model of Chen & Halpern (1989) has been used with success on many DPEs. However, an elliptical accretion disk (Eracleous et al. 1995) might arise if an instability is introduced in the disk, such as tidal disruption of a star or an orbiting

body (such as a second black hole, BH), which might allow an elliptical accretion disk to persist for some time (Syer & Clarke 1992). The disk profiles are typically centered around Balmer emission line positions presumably because of photoionization and electron scattering in the high-density medium of the disk. There is typically a peak on the red side and a peak on the blue side of the narrow emission lines. The specific shape of the line profile is dependent on geometrical factors such as the disk inclination, inner and outer radii, line broadening, and surface emissivity. The blue peaks can sometimes be stronger than the red peaks because of modest relativistic beaming.

Other configurations of an accretion disk can also produce similar double-peaked BL features. For example, asymmetric BL profiles can raise from non-uniformly distributed gas such as that in long-lived eccentric accretion disks (Ogilvie 2001). The warped accretion disk, produced by radiation-driven instabilities (Maloney et al. 1996), can generate the double-peaked line emission profile (Wu et al. 2008). In addition, a one-arm spiral excited by self-gravity in the accretion disk can also create asymmetry in the line profiles (Storchi-Bergmann et al. 2003). These configurations, although all capable of producing double-peaked BL features, predict different detailed line profiles and variability and can be tested by long-term spectroscopic monitoring (Gezari et al. 2007; Lewis et al. 2010). A few other complex scenarios involving two distinct orbiting SMBHs have also been proposed to explain a few individual DPEs with unusual profiles (Tang & Grindlay 2009; Barrows et al. 2011).

In this paper, we present the newly discovered DPE WISE J233237.05–505643.5 (W2332–5056, hereafter) at  $z = 0.3447$ . W2332–5056 has a radio luminosity of  $2.0 \times 10^{25}$  W Hz $^{-1}$  str $^{-1}$  at 4.85 GHz, comparable to other FR-II galaxies (Fanaroff & Riley 1974; assuming a spectral index  $\alpha = -0.8$  between 4.85 GHz and 178 MHz). The radio continuum morphology of this object is complex, exhibiting both FR-I and FR-II characteristics in addition to a winding primary jet with multiple structures near the core, including a linear structure perpendicular to the primary jet. The optical spectrum of W2332–5056 exhibits broad emission lines ( $H\alpha$  and  $H\beta$ ) blueshifted by  $\sim 3800$  km s $^{-1}$  with respect to the corresponding NLs. The combination of these features makes W2332–5056 a prime candidate for a SMBH merger system.

We describe the multi-band observations of W2332–5056 at mid-infrared (mid-IR), radio, optical, and X-ray wavelengths in Section 2. The detailed results comprise Section 3. In Section 4, we interpret our results and discuss various interpretations of this unusual object. We summarize our work in Section 5. Throughout this paper, we assume a concordance cosmology with  $H_0 = 70$  km s $^{-1}$  Mpc $^{-1}$ ,  $\Omega_m = 0.3$ , and  $\Omega_\Lambda = 0.7$ . For this cosmology, 1'' at  $z = 0.3447$  subtends 4.9 kpc.

## 2. SOURCE SELECTION AND OBSERVATIONS

W2332–5056 was identified based on its unusual mid-IR colors from the NASA *Wide-field Infrared Survey Explorer* (WISE; Wright et al. 2010). WISE mapped the entire sky in four mid-IR bands (3.4, 4.6, 12, and 22  $\mu$ m, or W1, W2, W3, and W4, respectively), achieving typical point-source sensitivities of 0.08, 0.11, 1, and 6 mJy (5 $\sigma$ ) in the four bands, respectively. In the short-wavelength bands, W2332–5056 has a relatively red [3.4]–[4.6] color of 0.9 mag, similar to normal AGNs (Stern et al. 2012) and occupies the same color–color space as other SMBH merger/recoiling candidates discussed in Section 1. However, its [4.6]–[12] color is 2.0 mag, significantly bluer than the typical AGNs seen by WISE (Jarrett

**Table 1**  
Multi-wavelength Photometry of W2332–5056

Band	R.A. (J2000.0)	Decl. (J2000.0)	Wavelength	Instrument	Flux Density	Epoch (UT)	Notes
Hard X-ray	23 <sup>h</sup> 32 <sup>m</sup> 37 <sup>s</sup>	-50°56'43"	2–10 keV	<i>Chandra</i> /ACIS	53 <sup>+8</sup> <sub>-7</sub> nJy <sup>a</sup>	2009 Aug 12, 30	
Soft X-ray	...	...	0.5–2 keV	...	63 <sup>+13</sup> <sub>-11</sub> nJy <sup>a</sup>	...	
FUV	23 <sup>h</sup> 32 <sup>m</sup> 36.89	-50°56'42.8"	1516 Å	<i>GALEX</i>	6 ± 3 μJy	[ 2003 Aug 10	
NUV	...	...	2267 Å	...	7 ± 2 μJy	] – 2005 Sep 6	
UKST- <i>B<sub>j</sub></i>	23 <sup>h</sup> 32 <sup>m</sup> 37.06	-50°56'43.2"	4400 Å	SuperCOSMOS <sup>a</sup>	26 ± 6 μJy	1975 Jul 16	
UKST- <i>R</i>	...	...	6600 Å	...	90 ± 20 μJy	1992 Nov 14	
UKST- <i>I</i>	...	...	8000 Å	...	80 ± 20 μJy	1991 Aug 3	
<i>g'</i>	23 <sup>h</sup> 32 <sup>m</sup> 36.96	-50°56'43.44	4770 Å	Magellan/IMACS <sup>b</sup>	85.1 ± 0.5 μJy	2008 Nov 3 and 4	
<i>r'</i>	...	...	6231 Å	...	182 ± 1 μJy	...	
<i>i'</i>	...	...	7625 Å	...	254 ± 1 μJy	...	
<i>z'</i>	...	...	9134 Å	...	432 ± 1 μJy	...	
<i>J</i>	23 <sup>h</sup> 32 <sup>m</sup> 37.06	-50°56'43.3"	1.235 μm	2MASS	0.37 ± 0.06 mJy	1999 Oct 18	
<i>H</i>	...	...	1.662 μm	...	0.42 ± 0.09 mJy	...	
<i>K<sub>s</sub></i>	...	...	2.159 μm	...	0.79 ± 0.09 mJy	...	
IRAC Channel 1	23 <sup>h</sup> 32 <sup>m</sup> 37.12	-50°56'44.1"	3.6 μm	<i>Spitzer</i> /IRAC	1.311 ± 0.002 mJy	2009 Nov 26	
W1	23 <sup>h</sup> 32 <sup>m</sup> 37.05	-50°56'43.5"	3.4 μm	WISE	1.31 ± 0.03 mJy	2010 May 19 and 20	
W2	...	...	4.6 μm	...	1.70 ± 0.04 mJy	...	
W3	...	...	12 μm	...	2.0 ± 0.1 mJy	...	
W4	...	...	22 μm	...	4 ± 1.0 mJy	...	
AKARI 9 μm		9 μm	AKARI	<0.03 Jy <sup>c</sup>	...	FWHM = 5'5	
AKARI 18 μm		18 μm	...	<0.05 Jy <sup>c</sup>	...	FWHM = 5'7	
IRAS 60 μm		60 μm	IRAS	<0.5 Jy	...	FWHM = 1'5 × 4'8	
IRAS 100 μm		100 μm	...	<1.5 Jy	...	FWHM = 3'0 × 5'1	
150 GHz		2 mm	SPT Survey <sup>d</sup>	<2.6 mJy <sup>c</sup>	...	FWHM = 1'	
9.0 GHz	23 <sup>h</sup> 32 <sup>m</sup> 37.06	-50°56'43.6"	3.3 cm	ATCA	37.2 ± 0.5 mJy <sup>e</sup>	2010 Jul 18 and 19	θ <sub>LAS</sub> = 2'3
5.6 GHz	23 <sup>h</sup> 32 <sup>m</sup> 37.05	-50°56'43.3"	5.4 cm	...	48.6 ± 0.3 mJy <sup>e</sup>	...	θ <sub>LAS</sub> = 3'9
1.5 GHz	23 <sup>h</sup> 32 <sup>m</sup> 36.86	-50°56'41.3"	20 cm	...	103 ± 2 mJy <sup>e</sup>	2010 Jul 16 and 17	θ <sub>LAS</sub> = 5'5
4.85 GHz	23 <sup>h</sup> 32 <sup>m</sup> 37.05	-50°56'43.5"	6.18 cm	PMN Survey <sup>f</sup>	47 ± 9 mJy	...	FWHM = 45''
843 MHz	23 <sup>h</sup> 32 <sup>m</sup> 36.62	-50°56'42.6"	35.6 cm	SUMSS <sup>g</sup>	175 ± 5 mJy	...	FWHM = 4'2

**Notes.**

<sup>a</sup> Corresponding to the observed  $f(0.5\text{--}2 \text{ keV}) = 2.32_{-0.32}^{+0.34} \times 10^{-13} \text{ erg cm}^{-2} \text{ s}^{-1}$  and  $f(2\text{--}10 \text{ keV}) = 1.01_{-0.17}^{+0.20} \times 10^{-12} \text{ erg cm}^{-2} \text{ s}^{-1}$ .

<sup>b</sup> Hambly et al. (2001).

<sup>c</sup> 3σ limit.

<sup>d</sup> Joaquin Vieira 2012, private communication.

<sup>e</sup> Integrated flux within a 0.5 radius.

<sup>f</sup> Gregory et al. (1994); Wright et al. (1994).

<sup>g</sup> Mauch et al. (2003).

et al. 2011). It is also a strong radio emitter, having been previously detected at 4.85 GHz in the Portes-MIT-NRAO (PMN) Survey (Gregory et al. 1994; Wright et al. 1994) and at 843 MHz in the SUMSS survey (Mauch et al. 2003). We obtained higher spatial resolution radio follow-up observations using the Australian Telescope Compact Array (ATCA) and optical imaging and spectroscopy with the Magellan, Southern Astrophysical Research (SOAR), and Gemini South (Gemini-S) telescopes. Details of the observations are given below.

W2332–5056 is 8.7 arcmin southeast (SE) of the background  $z = 0.5707$  galaxy cluster SPT-CL J2331–5051, which was discovered by the South Pole Telescope (SPT) Sunyaev–Zel'dovich survey (Vanderlinde et al. 2010). As a result, it has been observed with Magellan optical broadband imaging (Inamori Magellan Areal Camera and Spectrograph or IMACS; Dressler et al. 2011), the *Spitzer* IRAC camera, and the *Chandra* ACIS-I camera as part of SPT cluster follow-up programs. These observations are detailed below and the aperture photometry is presented in Table 1.

### 2.1. Radio Observations

The radio continuum observations were carried out at the ATCA using the Compact Array Broadband Backend with a

2×2 GHz bandwidth. W2332–5056 was mapped at 1.5 GHz in the 6C configuration on UT 2010 July 16 and 17. The 5.6 GHz and 9.0 GHz data were obtained simultaneously on UT 2010 July 18 and 19 in the 6C configuration (maximum baseline ∼6.0 km) and on UT 2010 August 10 in the hybrid H168 configuration (with five antennas closely positioned within 200 m of each other and the sixth antenna at a distance of 4.5 km). Observations were taken in snap-shot mode over 12 hr (6C) and 6 hr (H168) periods. A total of 25 minutes of integration was obtained at 1.5 GHz and 166 minutes at 9.0 and 5.6 GHz. PKS 1934-63 was used as the flux calibrator while PKS 2311-452 (for 5.6 and 9.0 GHz) and PKS 2333-528 (all three bands) were used for phase calibration. The largest angular scales ( $\theta_{LAS}$ ) visible under these configurations are 5'5 at 1.5 GHz, 3'9 at 5.6 GHz, and 2'3 at 9.0 GHz.

The data reduction was done using MIRIAD. The final robust weighted images are shown in Figures 1(a)–(c). The primary beam at the highest frequency, 9.0 GHz, is >6', significantly larger than the 1' field of interest for W2332–5056, and hence we did not apply a primary beam correction. The rms of the 1.5 GHz map is 0.62 mJy beam<sup>-1</sup> with a beam size of 13''.12 × 4''.80 and a position angle (P.A.) = 6°. The  $(u, v)$  data at 5.6 GHz and 9.0 GHz from the two configurations were combined,

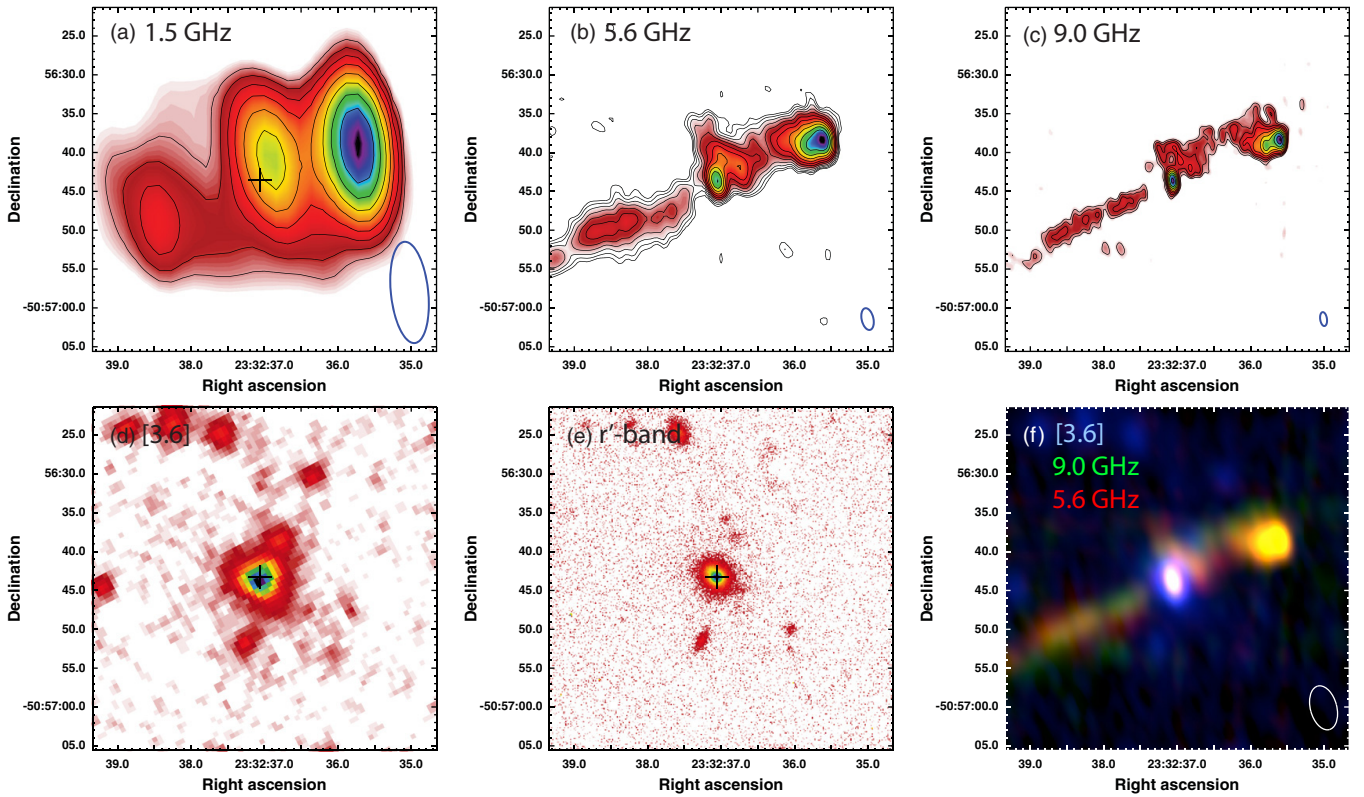


**Figure 1.** W2332–5056 imaging at radio, near-IR, and optical wavelengths. Images are in (a) 1.5 GHz continuum (beam size:  $13''.8 \times 4''.8$ , P.A. =  $6^\circ$ ), (b) 5.6 GHz continuum ( $2''.85 \times 1''.51$ , P.A. =  $13^\circ$ ), (c) 9.0 GHz continuum ( $1''.80 \times 0''.87$ , P.A. =  $8^\circ$ ), (d) *Spitzer* IRAC  $3.6\,\mu\text{m}$  (FWHM  $\sim 1''.7$ ), and (e)  $r'$ -band (seeing =  $0''.65$ ). In the radio maps (a)–(c), the colors represent the flux density from the peak in each map to the  $3\sigma$  level and the beam sizes of the maps are illustrated with blue ellipses in the lower-right corner of each panel. The contour levels are at  $2^{0.5n} \times 5\sigma$ , where  $n$  is a non-negative integer and  $1\sigma$  is at  $0.47\,\text{mJy}\,\text{beam}^{-1}$  at 1.5 GHz,  $0.026\,\text{mJy}\,\text{beam}^{-1}$  at 5.6 GHz, and  $0.034\,\text{mJy}\,\text{beam}^{-1}$  at 9.0 GHz. In the  $3.6\,\mu\text{m}$  (d) and  $r'$ -band images (e), the colors show the flux density peak from background levels on a logarithmic scale. The location of the 9 GHz radio core is marked with a “+” in (a), (d), and (e). The final panel (f) shows a composite mid-IR and radio view of W2332–5056 (blue: *Spitzer* IRAC  $3.6\,\mu\text{m}$ ; green: 9.0 GHz; red: 5.6 GHz) at matched resolutions ( $2''.9 \times 1''.7$ , P.A. =  $15^\circ$ ).

(A color version of this figure is available in the online journal.)

resulting in an rms noise of  $29\,\mu\text{Jy}\,\text{beam}^{-1}$  and  $37\,\mu\text{Jy}\,\text{beam}^{-1}$  in the final synthesized beams of  $2''.85 \times 1''.51$ , P.A. =  $13^\circ$  and  $1''.80 \times 0''.87$ , P.A. =  $8^\circ$ , respectively. The results of the integrated flux measurements using AIPS are listed in Table 1. Because the  $\theta_{\text{LAS}}$  for each band is larger than the angular extent of W2332–5056, we anticipate negligible or minimal missing flux in the ATCA interferometric measurements.

## 2.2. Mid-IR Observations

Table 1 presents mid-IR photometry of W2332–5056 from the *WISE* All-Sky Release Catalog (Cutri et al. 2012). The observations of this field were carried out on UT 2010 May 19 and 20. A total of 12 single frames in each *WISE* band are coadded. The spatial resolution of *WISE* is  $\sim 6''$  in W1, W2, and W3 and  $\sim 12''$  in W4. W2332–5056 is well detected in W1–W3, with a signal-to-noise ratio  $> 15$ , and marginally detected ( $4\sigma$ ) in W4. The mid-IR fluxes are listed in Table 1.

In addition, W2332–5056 was observed in W1 and W2 during the *WISE* post-cryogenic survey on UT 2010 November 13, 16, 17, and 18. A total of 19 frames were acquired, spread across 3 days due to the satellite maneuvering to avoid the Moon during its Sun-synchronous polar orbit. These second-epoch measurements allow us to test the variability of the AGN in W2332–5056 at mid-IR wavelengths, as discussed in Section 3.4.

Finally, due its projected proximity to SPT-CL J2331–5051, W2332–5056 was also observed in [3.6] during *Spitzer*

Cycle-9 (ID: 60099, PI: Mark Brodwin) on UT 2009 November 26. The pipeline-processed data (PBCD; shown in panel (d) of Figure 1), retrieved from the *Spitzer* Archive, provide another mid-IR epoch for comparison.

## 2.3. Optical and Near-IR Observations

### 2.3.1. Optical and Near-IR Imaging

Optical photometry of W2332–5056 was obtained with Magellan-IMACS in the SDSS  $g'r'i'z'$ -bands as part of SPT cluster follow-up efforts (Vanderlinde et al. 2010). The observations were taken on UT 2008 November 3 and 4 with a median seeing of  $\sim 0''.8$  and the  $5\sigma$  magnitude limits in the AB system are  $\sim 24.8$ , 24.8, 24.4, and 23.4 for  $g'$ ,  $r'$ ,  $i'$ , and  $z'$ , respectively. The details of the Magellan observations and data reduction are described in High et al. (2010).

To explore variability, we obtained archival photometric data of W2332–5056 from several major sky surveys. The optical photometry from SuperCOSMOS Sky Survey (Hamby et al. 2001) in UKST  $B_J$ ,  $R$ , and  $I$ -bands has a photometric uncertainty of  $\sim 0.3$  mag. Near-IR imaging from the Two Micron All Sky Survey (2MASS; Skrutskie et al. 2006) was obtained on UT 1999 October 18 and provided  $5\text{--}9\sigma$  detections in the  $J$ ,  $H$ , and  $K_S$ -bands. Detailed information of these sky survey observations is presented in Table 1.

In order to study the morphology of W2332–5056, we also acquired high-quality  $r'$ -band imaging ( $\bar{\lambda} \sim 6165\,\text{\AA}$ ) with  $0''.65$

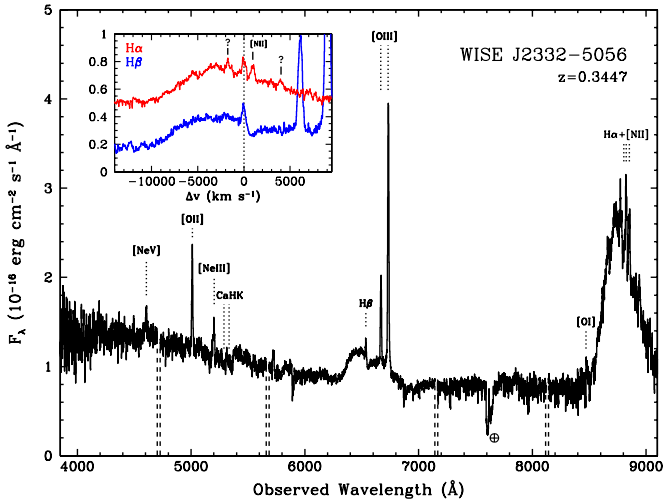


**Figure 2.** Combined GMOS-S optical spectrum of W2332–5056 from 3800–9100 Å. The NLs are marked at redshift  $z = 0.3447$ . The “+” symbol labels atmospheric absorption features. The scaled broad H $\alpha$  and H $\beta$  lines are highlighted in the inset panel, indicating velocities relative to the NL redshift (shown by the dotted vertical line). The dashed lines around 4715 Å, 5675 Å, 7155 Å, and 8130 Å represent the CCD gaps of GMOS. The “?” symbols mark unidentified narrowband features.

(A color version of this figure is available in the online journal.)

seeing using the 4.1 m SOAR telescope with the SOAR Optical Imager (Walker et al. 2003) on UT 2011 November 22. The basic image processing and reductions were carried out with IRAF. This  $r'$ -band image is shown in panel (e) of Figure 1.

### 2.3.2. Optical Spectroscopy

The optical spectroscopic observations of W2332–5056 were carried out with the Gemini Multi-Object Spectrograph (GMOS; Hook et al. 2004) on the Gemini-S telescope on UT 2011 May 11 and UT 2011 November 28. We obtained two 10 minute integrations observations with the 1''.5 slit and the B600/520.0 disperser in 2011 May, covering 3800–6700 Å with a resolving power  $R \equiv \lambda/\Delta\lambda = 1700$ . At  $z = 0.3447$ , the H $\beta$  line is near the red end of the wavelength coverage. In 2011 November, in order to cover H $\beta$  and H $\alpha$  together and confirm the BL H $\beta$  feature observed earlier, we revisited W2332–5056 with Gemini-S/GMOS, with the 1''.5 slit and the R400/705.0 disperser. The wavelength coverage ranged from 6200 Å to 9100 Å with  $R = 1900$ . The spectra were processed using IRAF. The white dwarf GJ 318 was used for flux calibration in 2011 May and the DA white dwarf LTT3218 was used in 2011 November. The final combined spectrum is shown in Figure 2.

### 2.4. X-Ray Observations

W2332–5056 was serendipitously observed twice with the ACIS-I camera in programs to map the galaxy cluster SPT-CL J2331–5051. The total exposure time was 35.0 ks, split between a guaranteed time observation of 29.0 ks on UT 2009 August 12 (ObsID 9333; PI: Garmire) and a guest observation of 6.0 ks on UT 2009 August 30 (ObsID 11738; PI: Mohr). The X-ray data for the cluster were reported in Andersson et al. (2011). The data were analyzed following standard procedures using the *Chandra* Interactive Analysis of Observations (CIAO; V4.2) software. We identified “good time intervals” for the observations, yielding a total effective exposure time of 30.0 ks for W2332–5056.

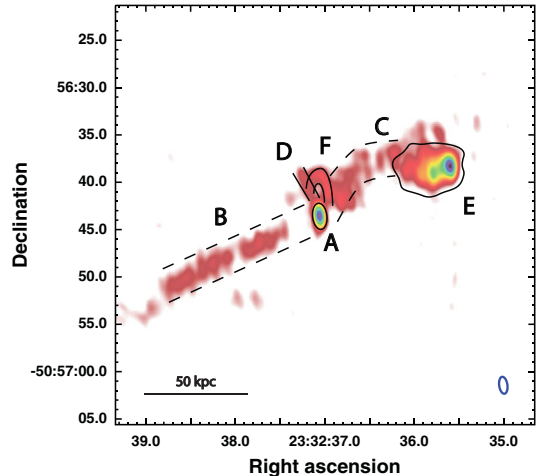


**Figure 3.** 9.0 GHz continuum map with the key radio features illustrated: (A) core, (B) primary SE jet, (C) primary counter NW jet, (D) linear structure, (E) hot spot, and (F) arc-like structure.

(A color version of this figure is available in the online journal.)

**Table 2**  
Radio Continuum Flux Densities of Resolved Radio Components

Component	ID	$F_{1.4\text{ GHz}}$ (mJy)	$F_{5.6\text{ GHz}}$ (mJy)	$F_{9.0\text{ GHz}}$ (mJy)	$\alpha_{9.0}^{5.6}$
Core	(A)	$14 \pm 1$	$5.0 \pm 0.1$	$4.6 \pm 0.1$	$-0.18 \pm 0.07$
Primary jet (SE)	(B)	$34 \pm 1$	$11.6 \pm 0.2$	$9.5 \pm 0.3$	$-0.41 \pm 0.08$
Primary jet (NW)	(C)	$57 \pm 1$	$27.8 \pm 0.2$	$18.1 \pm 0.3$	$-0.90 \pm 0.03$
Linear structure	(D)	...	$1.5 \pm 0.1$	$1.1 \pm 0.1$	$-0.70 \pm 0.15$
Hot spot	(E)	...	$21.2 \pm 0.1$	$14.0 \pm 0.2$	$-0.87 \pm 0.03$
Arc-like structure	(F)	...	...	$1.83 \pm 0.08^a$	...

**Notes.** Component IDs (second column) are marked in Figure 3.  $F_{5.6\text{ GHz}}$  and  $F_{9.0\text{ GHz}}$  are measured in the beam-matched maps ( $2''.9 \times 1''.6$ , P.A. =  $15^\circ$ ).  $\alpha$ , as defined in  $F_v \propto \nu^\alpha$ , is the spectral index between 9.0 GHz and 5.6 GHz.

<sup>a</sup> Measured in the map of the beam =  $1''.80 \times 0''.87$ , P.A. =  $8^\circ$ .

## 3. RESULTS AND ANALYSES

### 3.1. Radio Continuum Morphology

The ATCA maps at 1.5 GHz (20 cm), 5.6 GHz (5.4 cm), and 9.0 GHz (3.3 cm) are shown in panels (a)–(c) of Figure 1. These maps clearly show a mixed morphology between FR-I and FR-II structures that comprise the W2332–5056 system. In the lowest resolution map, at 1.5 GHz ( $3'' \times 4''$ ), three distinct peaks are observed, including the core and two unevenly bright spots at both ends of the center. The central peak is offset by  $3''.0$  from the location of the WISE-detected host galaxy (referred to as the core), which indicates significant unresolved 20 cm emission from the extended structure north of the core. At shorter wavelengths, the jet is well resolved and exhibits a complex morphology, described next.

In the 9.0 GHz map ( $1''.80 \times 0''.87$ , P.A. =  $8^\circ$ ), we identify six distinguishable components, marked as A–F in Figure 3: (A) a core (coincident with the host galaxy), a pair of “primary” jets, including (B) a SE jet with a P.A. of  $120^\circ$  and (C) the counter distorted northwest (NW) jet, (D) a linear structure at a nearly orthogonal P.A. of  $20^\circ$ , (E) a luminous hot spot, and (F) an arc close to the core. The fluxes of these radio structures are listed in Table 2.

At the position of the mid-IR and optical peak, a radio core is apparent. The core has a relatively flat spectrum: a spectral

index of  $\alpha = -0.18 \pm 0.07$  ( $F_v \propto v^\alpha$ ) from 5.6 GHz to 9.0 GHz in the maps of matched beam of  $2''.9 \times 1''.6$  at P.A. =  $15^\circ$ . The deconvolved size of the core is  $< 0''.3$  at 9.0 GHz, based on single Gaussian fitting of the uniformly weighted map.

Originating from the core, the primary jet extends about  $14''$  to the NW, punctuated by a typical FR-II galaxy Doppler-boosted hot spot that is much brighter than the core. In contrast to the linear jet (“B”) to the SE, the NW jet shows an asymmetric zig-zag morphology. The deviation is  $10^\circ$  from the axis of the SE jet, while a deviation of  $30^\circ$  is seen on the opposite side. Moreover, there appear to be distinct differences across the radio bands, notably closer to the core, better revealed in Figure 1(f). The jet is more curved at 5.6 GHz on the SE side and relatively straighter on the NW, spatially offset from the 9.0 GHz emission. The nature of this offset is under investigation with new, deeper radio observations that we are currently pursuing.

The faint linear structure “D,” pointing to the center of the core, extends  $5''\text{--}7''$  from the central core, is visible at 5.6 GHz, and notably at 9.0 GHz (appearing as “green” in Figure 1(f)), extending over  $>2$  beams. The emission at 1.5 GHz is also extended in the same direction, indicated by the elongation of the core in the low resolution 1.5 GHz map. The coalignment is shown in both 9.0 GHz and 5.6 GHz of the radio core and the resolved host in optical imaging (white/magenta in the figure). This structure has signal-to-noise  $>30$ . It is at a P.A. of  $20^\circ$ , which is distinct from the P.A. of the elongated ATCA beams at 5.6 GHz and 9.0 GHz ( $13^\circ$  and  $8^\circ$ , respectively). Moreover, it does not match the uncleared dirty beam structure of a relatively weak central core (the peak-to-peak ratio between the core and component “D” is  $\sim 8$ ). Structure “F” has an unusual shape resembling a curved, arc-like structure, possibly the result of a three-dimensional radio structure seen in projection.

The primary jets extend to 70 kpc on both sides at a P.A. of  $120^\circ$ . To our detection limit, there is no clear jet-like structure that connects directly to the core on the axis of the primary jet in the central 12 kpc ( $2''.5$ ). The western jet exhibits a complex behavior that may indicate interactions with the ISM and intergalactic medium. The structure of the eastern counterjet is more linear, with a maximum P.A. change of  $\lesssim 10^\circ$ . The pitch angle along the jet reaches  $20^\circ$  in the 5.6 GHz map, whereas it is within  $5^\circ$  at 9.0 GHz. If the driving mechanism that produces this “zig-zag” morphology in the jets is periodic, the estimated period is on the order of 0.25 Myr based on the length between off-axis peaks of the serpentine primary jet.

The asymmetric brightness of the jets suggests that the western side of the primary jet is on the side near to us. This is because jets can be brighter (fainter) by a factor of  $D^3$  if they are moving toward (away from) the observer (discussed in Meier et al. 2001), where  $D \equiv [\Gamma(1 + (v/c)\cos\theta)]^{-1}$  is the Doppler factor for a relativistic jet at Lorentz factor  $\Gamma$  for given velocity  $v$  and the angle between the axis of the jet and the observer’s line of sight  $\theta$ . However,  $\theta$  for the primary jets is likely to be  $> 80^\circ$  (e.g., the maximum for jets in the face-on plane) based on the relatively small brightness difference between the primary jets on each side.

### 3.2. Spectroscopy: Broad H $\alpha$ and H $\beta$ Emission Lines

The integrated fluxes of identified lines are listed in the Table 3. The presence of the high ionization line [Ne V]3426 Å, as well as the ratio of [O III]5007 Å to NL H $\beta$  indicate the AGN nature of W2332–5056. Additional evidence for an AGN is provided by broad H $\alpha$  and H $\beta$  line widths, as shown in Figure 2. Both have asymmetric profiles with respect to the NL. The

**Table 3**  
Optical Line Fluxes of W2332–5056

Line	Redshift	Flux ( $10^{-16}$ erg cm $^2$ s $^{-1}$ )
[Ne V] $\lambda 3426$	0.3439	$7.0 \pm 0.6$
[O II] $\lambda 3727$	0.3443	$13.4 \pm 0.4$
[Ne III] $\lambda 3869$	0.3440	$6.8 \pm 0.4$
[O III] $\lambda 4363$	...	$1.2 \pm 0.3^a$
He II $\lambda 4686$	...	$0.8 \pm 0.3^a$
H $\beta$		
NL	0.3447	$2.12 \pm 0.2$
BL-blue	...	$64.1 \pm 0.8^b$
BL-red	...	$71.8 \pm 1.0^c$
[O III] $\lambda 4959$	0.3449	$11.2 \pm 0.2$
[O III] $\lambda 5007$	0.3449	$42.2 \pm 0.2$
[O I] $\lambda 6300$	0.3458	$4.4 \pm 0.7$
H $\alpha$		
NL	0.3447	$12.8 \pm 0.6$
BL-blue	...	$436 \pm 3^b$
BL-red	...	$265 \pm 2^c$
[N II] $\lambda 6583$	0.3448	$10.5 \pm 0.6$

#### Notes.

<sup>a</sup> Marginal detection.

<sup>b</sup> Integrated flux from zero velocity to the blue end of the BL component.

<sup>c</sup> Integrated flux from zero velocity to the red end of the BL component.

FWHM of H $\alpha$  is  $\sim 11,000$  km s $^{-1}$ , and the full width at quarter maximum is  $\sim 16,000$  km s $^{-1}$ . For H $\beta$ , the peak of the BL component is centered at  $\sim 6453$  Å or  $3800$  km s $^{-1}$  blueshifted with respect to the systemic host galaxy redshift of 0.3447, consistently measured by both the narrow emission lines as well as the CaHK absorption. Similarly, the peak of the BL H $\alpha$  is at  $8730$  Å or  $3200$  km s $^{-1}$  blueshifted with respect to the host galaxy systemic redshift. Objects with asymmetric, very broad Balmer lines whose peaks are shifted from the corresponding NLs are usually referred to as DPEs. We note a few narrow emission features (marked as “?” in the inset of Figure 2) straddling H $\alpha$ , unlikely to be [N II] or [S II], which could potentially be associated with H $\alpha$  components shifted by  $-1700$  and  $+4000$  km s $^{-1}$  with respect to the galaxy systemic velocity. The different blueshifts for the broad H $\alpha$  and H $\beta$  are the result of contamination from these unidentified components. From the difference between the scaled H $\alpha$  and H $\beta$  profiles, we detect no significant broad Fe II emission near H $\beta$  within  $\pm 10,000$  km s $^{-1}$ . We do not see clear evidence for very BL regions in other spectral features.

#### 3.2.1. Parameterization with Gaussian Profiles

We first attempted to parameterize the BL components with two Gaussian profiles without excluding narrow emission lines in order to measure the FWHM and fluxes of all lines. The two BL Gaussian profiles and one NL component are used for both H $\alpha$  and H $\beta$  in the model, allowing us to fit independently H $\beta$  and H $\alpha$ . The narrow absorption features (between rest-frame 4866.4–4908.2 Å and 6529.3–6552.4 Å) are excluded from the fitting process. For the [O III]4959 Å and 5007 Å lines, one BL Gaussian component and one NL component are assumed, while the [N II]6583 Å is fit with a single NL Gaussian component. The redshift and linewidth of the [O III]4959 Å and [O III]5007 Å lines are assumed to be equal, with a fixed flux

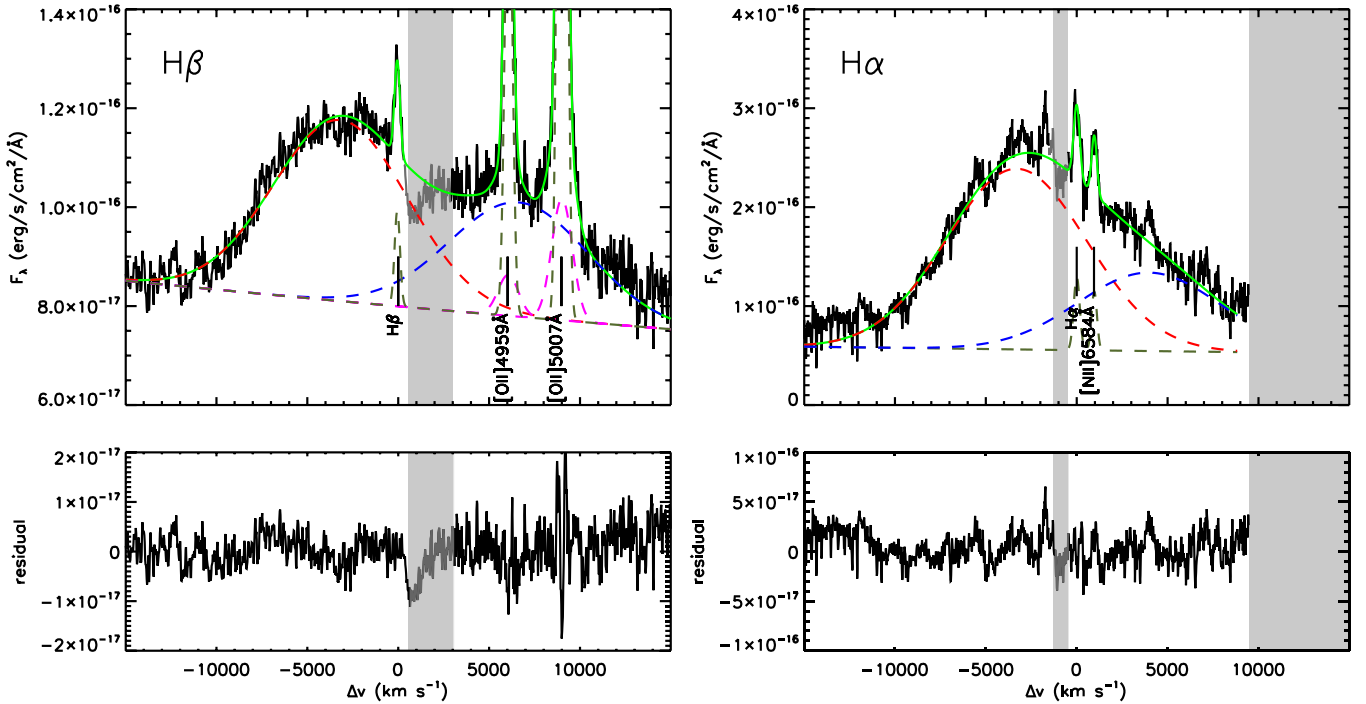


**Figure 4.** Observed  $H\beta$  and  $H\alpha$  BLs overplotted with the best-fit Gaussian models of BLs plus NLs. The two Gaussian BL profiles in the model are fit independently to both  $H\beta$  and  $H\alpha$ . The redshift and linewidth of [O III]4959 Å and [O III]5007 Å are assumed to be equal, with a fixed flux ratio  $F_{[O\text{ III}]\text{5007}}/F_{[O\text{ III}]\text{4959}} = 3$ . The shaded regions, which cover the narrow absorption features and wavelengths outside the spectral window, are excluded in the model fitting. The blue and red dashed lines represent the blueshifted and redshifted BL components of  $H\alpha$  and  $H\beta$ , respectively. The magenta lines indicate the BL components of [O III]4959 Å and [O III]5007 Å. The dark green dotted lines show NL components of the  $H\beta$ , [O III]4959 Å, [O III]5007 Å,  $H\alpha$ , and [N II]6584 Å lines. The green solid line is the sum of all components. The lower two panels show the residuals from the fitting.

(A color version of this figure is available in the online journal.)

**Table 4**  
Emission Line Parameters

Line	$\Delta V$ (km s $^{-1}$ )	FWHM (km s $^{-1}$ )	Flux ( $10^{-16}$ erg cm $^2$ s $^{-1}$ )
$H\alpha$			
NL	$0 \pm 40$	$390 \pm 50$	$9 \pm 1$
BL-blue	$-4410 \pm 50$	$9180 \pm 30$	$519 \pm 2$
BL-red	$+5330 \pm 130$	$9110 \pm 60$	$229 \pm 3$
$H\beta$			
NL	$-70 \pm 30$	$360 \pm 60$	$1.6 \pm 0.2$
BL-blue	$-4270 \pm 90$	$8790 \pm 10$	$74 \pm 1$
BL-red	$+8860 \pm 130$	$8800 \pm 20$	$48 \pm 1$
[O III] $\lambda 5007$			
NL	$+70 \pm 10$	$480 \pm 10$	$33 \pm 1$
BL	$+50 \pm 50$	$1300 \pm 120$	$8 \pm 1$
[N II] $\lambda 6583$			
NL	$-10 \pm 10$	$340 \pm 60$	$6 \pm 1$

**Notes.** The results of Gaussian fitting of the emission lines. The second column,  $\Delta V$ , represents the velocity offset with respect to the rest-frame wavelength of the line at a redshift of 0.3447. For each emission line, one BL component and one NL component is included, except for  $H\alpha$  and  $H\beta$ , for which two BL components are employed. The [O III]4959 Å (not shown in the table) and [O III]5007 Å lines are forced to have the same  $\Delta V$  and FWHM, with a 1:3 line flux ratio.

ratio  $F_{[O\text{ III}]\text{5007}}/F_{[O\text{ III}]\text{4959}} = 3$ . The results ( $\chi^2_{\text{red}} = 1.85$ , degrees of freedom (dof) = 3607) are shown in Figure 4 and Table 4.

The blue BL components are centered at  $\lesssim -4300$  km s $^{-1}$  with respect to the NL, while the red component peaks at  $> +5300$  km s $^{-1}$ . Both blue and red BL components have FWHMs  $\gtrsim 8800$  km s $^{-1}$ . The flux of the blue components

is  $\sim 1.5\text{--}2.3$  times that of the red components. The fitting residuals shown in the lower panels of Figure 4 indicate that the model represents the data near both  $H\alpha$  and  $H\beta$  fairly well, except for the blocked region and the very red wing of  $H\beta$  ( $\Delta V > 11,000$  km s $^{-1}$ ).

### 3.2.2. Spectroscopic Modeling—The Case of a Thin, Elliptical Accretion Disk

In the literature, the DPE feature, such as we see in W2332–5056, has often been interpreted as a thin accretion disk surrounding a single AGN (Bonning et al. 2007; Shields et al. 2009; Eracleous et al. 2009). We test the disk-emitter scenario by fitting the  $H\alpha$  and  $H\beta$  profiles with models based on line emission from an elliptical accretion disk (Eracleous et al. 1995). The asymmetric blueshifted BL features in both  $H\alpha$  and  $H\beta$  in this model are due to Doppler-boosted line emission from the disk. All NL features ( $H\alpha$ ,  $H\beta$ , [O III]4959 Å, [O III]5007 Å, [N II]6584 Å) and an unexpected “absorption-like” region redward of NL  $H\beta$  (6535–6600 Å) are excluded from the model fitting. The eccentricity,  $e$ , angle of periastron,  $\phi$ , inclination angle,  $i$ , and inner/outer radii,  $r_{\text{in}}/r_{\text{out}}$ , are free parameters for fitting. Each model fit  $H\alpha$  and  $H\beta$  with a radius-dependent power-law emissivity  $\epsilon(r) = \epsilon_0 \times r^{-q}$  for the disk, where  $r$  is the radius of the emission region from the center and  $q$  is the power-law index. Two  $q$  indices are used as independent parameters,  $q_{H\alpha}$  and  $q_{H\beta}$ , for the emissivities of  $H\alpha$  and  $H\beta$ , respectively. These emissivity assumptions for the photoionization models (Collin-Souffrin & Dumont 1989; Dumont & Collin-Souffrin 1990a, 1990b) were developed by Chen & Halpern (1989) and are extensively used by others, including Eracleous & Halpern (2003).

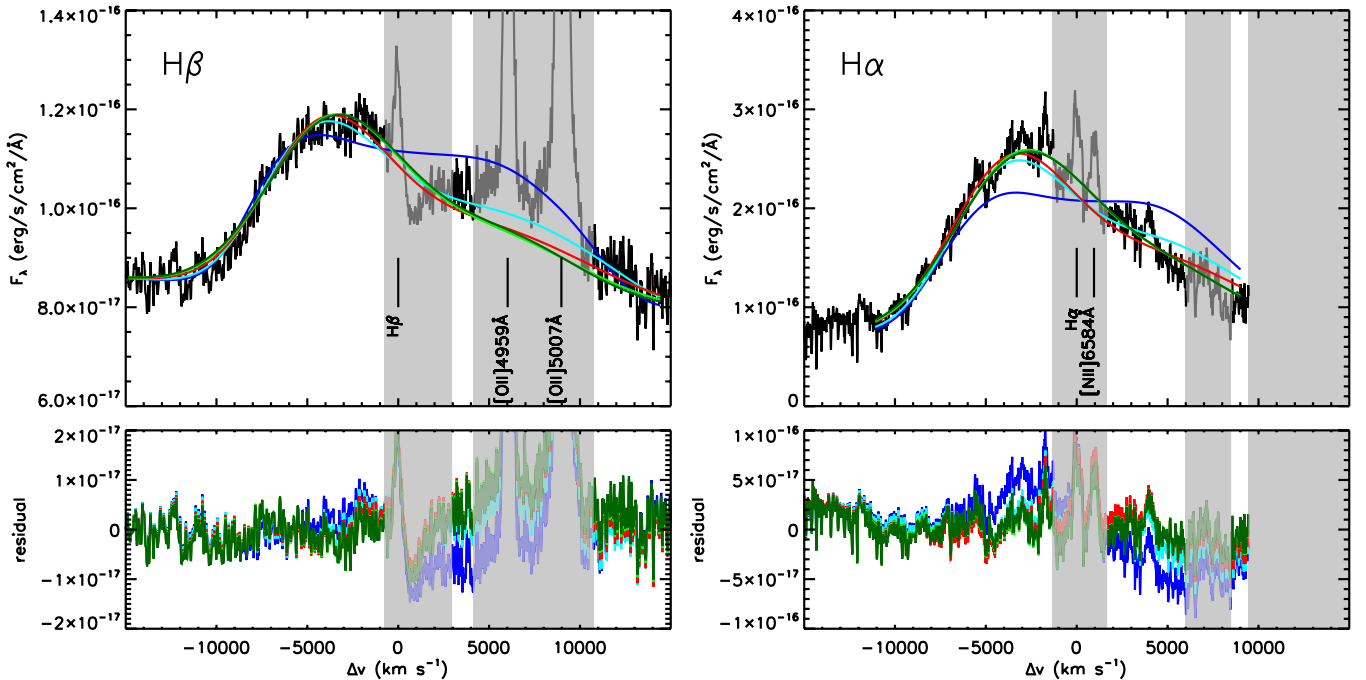


**Figure 5.** Observed H $\beta$  and H $\alpha$  BLs overplotted with elliptical disk models for five eccentricities with all other parameters the same:  $e = 0.0$  (blue),  $e = 0.2$  (cyan),  $e = 0.4$  (red),  $e = 0.6$  (green), and  $e = 0.8$  (dark green). Models are fit simultaneously to both H $\beta$  and H $\alpha$  with an assumption of a radius-dependent power-law emissivity. See the text for details. The shaded regions are excluded in the model fitting. The  $e = 0.6$  model yields the best fit, although the BL profiles can be fit relatively well by the  $e = 0.2, 0.4$ , and  $0.8$  models.

(A color version of this figure is available in the online journal.)

The modeling was performed by fitting a grid of free parameters and adopting the set of parameters that yields the lowest reduced  $\chi^2$  value. We tested elliptical disk models for eccentricities of  $e = 0.0\text{--}0.8$  (shown in Figure 5 along with the best-fit circular model). The high eccentricity  $e = 0.6$  model provides a statistically significant improvement to explain the BL profiles ( $\chi^2_{\text{red}} = 0.88$ , dof = 1887), although models with  $e > 0.2$  generally provide a good fit ( $\chi^2_{\text{red}} \leq 1.02$ ). The best-fit parameters of this model are as follows:  $e = 0.6$ ,  $q_{H\alpha} = 2.4$ ,  $q_{H\beta} = 3.2$ ,  $i = 42^\circ$ , FWHM local broadening  $\sigma = 3300 \text{ km s}^{-1}$ ,  $r_{\text{disk}}^{\text{inner}} = 240r_G$ , and  $r_{\text{disk}}^{\text{outer}} = 4500r_G$ , where  $r_G$  is the Schwarzschild radius of the central BH.

This model with a thin disk and offset BL regions can reasonably explain the H $\alpha$  and H $\beta$  line profiles in W2332–5056, other than an apparent “absorption” feature at  $\Delta V \sim 1000 \text{ km s}^{-1}$  redshifted with respect to H $\beta$ . This absorption-like profile is not observed for H $\alpha$ , likely because it overlaps with [N II]6583 Å emission at the systemic redshift of the galaxy. The nature of this feature is yet unknown.

### 3.3. X-Ray Emission

The AGN hosted by W2332–5056 is strongly detected in *Chandra* ACIS-I data, with a total of 1790 source counts in the energy range 0.3–7 keV. It is the brightest X-ray source in the field. In the deeper observation (ObsID 9333), our target is 9.3 off-axis, where the *Chandra*/ACIS 50% encircled energy radius is 4'' at 1.4 keV. We extracted the source distorted by the off-axis point-spread function (PSF) using a relatively large 12'' radius circle. The background was from a 30'' circular, source-free region. Response matrices and effective areas were then determined for the target position and the spectrum was binned to have at least 20 counts per spectral bin. The resulting spectrum was analyzed using XSPEC (V12.6.0).

W2332–5056 appears spatially extended in the *Chandra* data, but the distorted off-axis PSF complicates the interpretation of this spatial structure. We used the CIAO task ARESTORE to perform PSF deconvolution on the deeper image (ObsID 9333) with a PSF simulated by Chart in the energy range of 0.3–7 keV. Two weak, extended X-ray regions  $\sim 4.5''$  from the central X-ray peak at P.A.s of  $\sim 30^\circ$  and  $\sim 200^\circ$  are marginally detected; together they contain  $\sim 0.6\%$  of the X-ray photon counts.

Using the standard definition of hardness ratio,  $\text{HR} \equiv (H - S)/(H + S)$ , where  $H$  is the hard counts between 2–10 keV and  $S$  is the soft counts between 0.5–2 keV, the derived  $\text{HR} = -0.05$  is typical of extragalactic X-ray sources (e.g., Stern et al. 2002). Our best absorbed power-law fit ( $\chi^2_{\text{red}} = 1.09/70$  dof) to the spectrum has an observed photon index  $\Gamma = 1.51 \pm 0.08$ , a total absorbing column of  $N_H = 5.31^{+0.92}_{-0.86} \times 10^{21} \text{ cm}^{-2}$ , an observed soft X-ray flux of  $f(0.5\text{--}2 \text{ keV}) = 2.32^{+0.34}_{-0.32} \times 10^{-13} \text{ erg cm}^{-2} \text{ s}^{-1}$ , and an observed hard X-ray flux of  $f(2\text{--}10 \text{ keV}) = 1.01^{+0.20}_{-0.17} \times 10^{-12} \text{ erg cm}^{-2} \text{ s}^{-1}$ . The corresponding intrinsic, or unobscured, X-ray luminosities are  $L(0.5\text{--}2 \text{ keV}) = 1.72^{+0.06}_{-0.06} \times 10^{44} \text{ erg s}^{-1}$  and  $L(2\text{--}10 \text{ keV}) = 4.14^{+0.32}_{-0.28} \times 10^{44} \text{ erg s}^{-1}$ .

### 3.4. Variability

W2332–5056 was observed in *Spitzer* [3.6] in 2009 and in *WISE* [3.4] between 2010–2011. The median of the [3.4] single-frame fluxes is  $1.30 \pm 0.05 \text{ mJy}$  while the [3.6] flux from a single measurement is  $1.311 \pm 0.002 \text{ mJy}$ ; the anticipated color difference between IRAC [3.6] – *WISE* [3.4] is less than 0.1 mag.<sup>14</sup> No significant mid-IR variation is seen.

<sup>14</sup> Based on Figure 4 of [http://wise2.ipac.caltech.edu/docs/release/allsky/expsup/sec6\\_3a.html](http://wise2.ipac.caltech.edu/docs/release/allsky/expsup/sec6_3a.html)

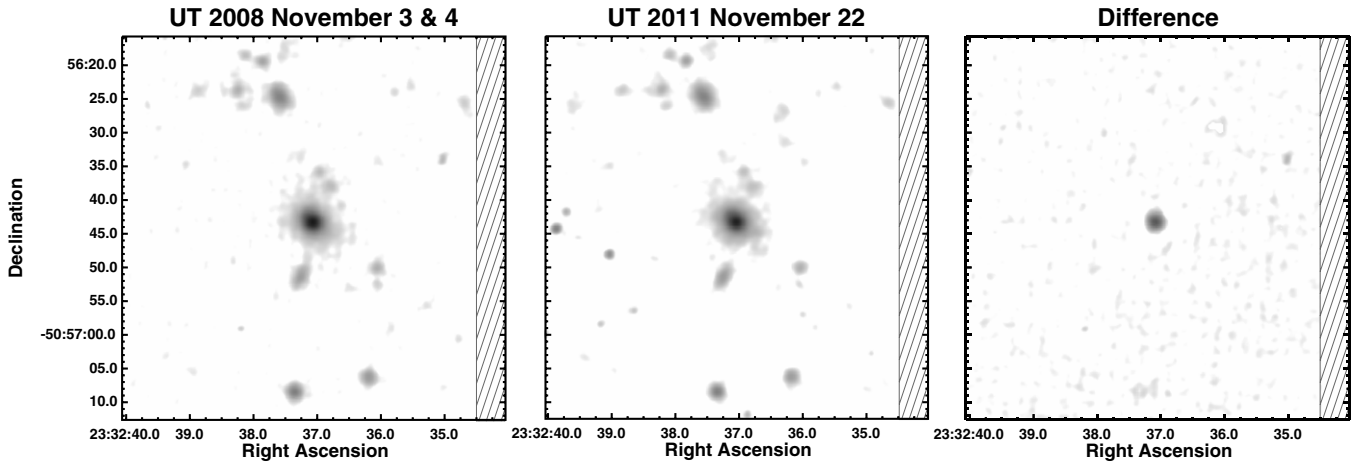


**Figure 6.** Optical \$r'\$ images of W2332–5056 from two different epochs (left two panels) after convolving to a matched 1''.2 FWHM PSF and the residual difference image (right panel). The shaded region illustrates the region in the CCD gap in the 2011 observations. This region is excluded in the analysis. All 5\$\sigma\$ sources, including the extended structure of W2332–5056, are successfully subtracted down to the <2\$\sigma\$ level. The residual component of W2332–5056, coincident with the nucleus, has a FWHM of 1''.2, indicating that it is unresolved. The peak flux of the residual is \$\sim\$140\$\sigma\$ of the difference image and contains about 18% of the flux of the peak in 2008 November, which is brighter than that in 2011.

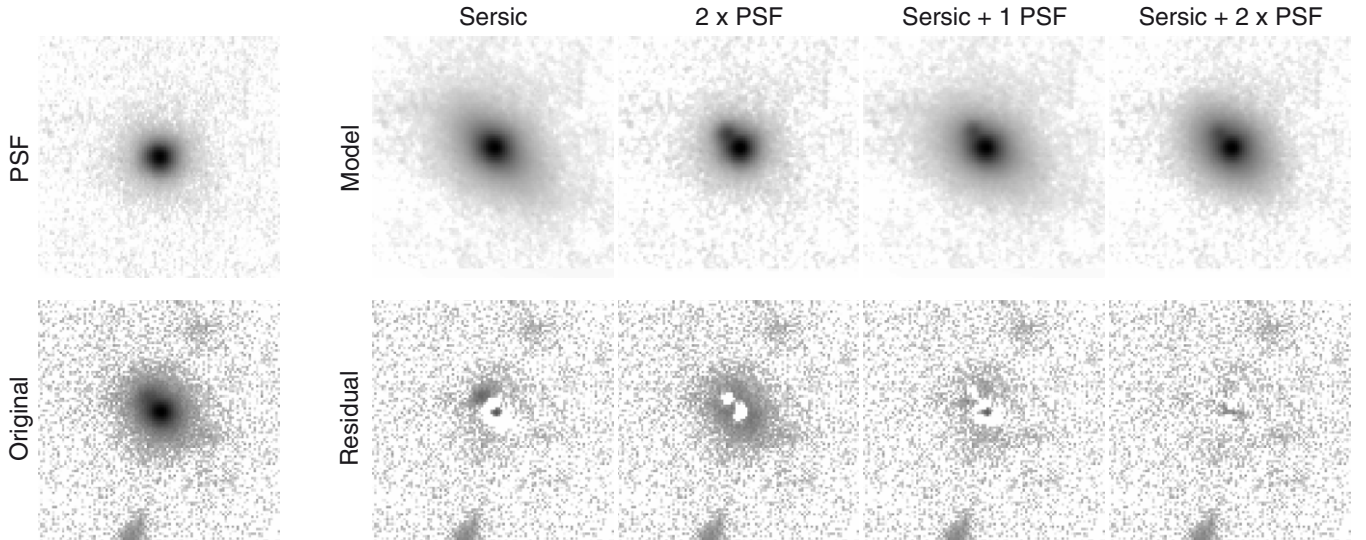


**Figure 7.** GALFIT morphological models and residuals images of W2332–5056 in the \$r'\$ band. The PSF and the original image (taken on UT 2012 November 22 with a seeing of 0''.65) are shown on the left. The other eight panels, in square-root scale, show models and residual images (14'' on a side). Note that the free single PSF component in the “Sérsic + 1 PSF” model (the second column from the right) selects an off-center optical bright spot instead of the central peak.

At optical wavelengths, the redshifted H\$\beta\$ spectra were obtained twice in 2011, separated by six months. There is no obvious variation in H\$\beta\$ between these two epochs. On longer time spans (>3 yr), the central AGN does show significant fluctuations at optical wavelengths. The residual in the differential \$r'\$-band imaging (Figure 6) indicates a \$\sim\$20% total flux decrease from 2008 November to 2011 November.

### 3.5. Optical Imaging Morphology

W2332–5056 is clearly resolved in the SOAR \$r'\$-band image (see Figures 1(e) and 7; 0''.65 seeing). We use GALFIT 3.0 (Peng et al. 2002, 2010) to examine its morphology. Inspired by evidence of at least one BL AGN in the system, we use a combination of Sérsic profiles and PSFs to model the host galaxy and unresolved AGN components, respectively. The results are shown in the right panels of Figure 7. The single Sérsic model, single PSF model, and dual PSF models cannot explain the observed morphology; all of them leave significant residual flux (>3%) within a 4''.8 radius of the core. Modeling the image with

a Sérsic profile plus a single free PSF, the PSF preferentially selects an off-center optical bright spot, but leaves significant central residual flux (\$\sim\$7%). The best-fit model (\$\chi^2\_{\text{red}} \sim 1.4\$, dof = 40388) requires a single Sérsic profile accompanied with two PSF profiles that match the observed brightness distribution to <0.5%. In this model, the Sérsic component, primary PSF component, and secondary PSF components contribute 33.7%, 61.8%, and 4.5% of the total flux, respectively.

The Sérsic profile (of the host galaxy) in the best-fitted model has an axis ratio of 0.64 at a P.A. of 48°. It contributes \$\sim\$50 \$\mu\$Jy (or AB = 19.64) with an effective radius of 1''.36 (6.7 kpc) and has a Sérsic index of 0.92, close to an exponential disk index \$n = 1\$. This component has \$M\_{r'} = -21.6\$ (AB mag) before \$k\$ corrections, slightly brighter than the Milky Way. The luminosity is \$2.5 \times 10^{10} L\_\odot\$, similar to our spectral energy distribution (SED) model of the host galaxy (blue line in Figure 8). The primary PSF component is centered 0''.16 offset (\$\sim\$800 pc in projection) from the Sérsic center. This displacement, 25% of the PSF FWHM, appears significant, but could be the result

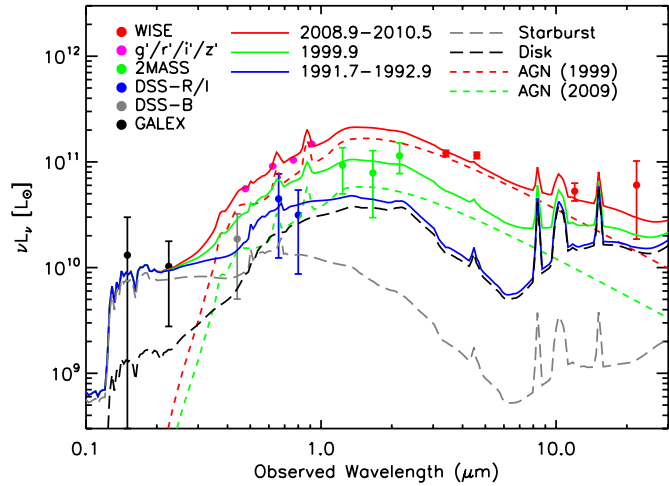


**Figure 8.** UV-IR SED models of W2332–5056. The dashed lines represent the different components in the SED, including starburst (gray), normal disk (black), and AGN (red and green), based on the empirical SED templates from Assef et al. (2010). Because of the variability among the different epochs (see Section 3.4), we separate the fitting into three different epochs: 1991 August–1992 November (GALEX + DSS; blue), 1999 October (GALEX + 2MASS; green), and 2008 November–2010 May (GALEX +  $g'r'i'z'$  + WISE; red). The DSS  $B$  data (gray dot) taken in 1975 are not included in the fitting. The UV data from GALEX are fixed for fitting all epochs (see the text for details). The earliest epoch data (blue solid line) are well fit by a galaxy without any AGN component. The later two epochs (green and red solid lines) are fit by adding an AGN component that brightens over time.

(A color version of this figure is available in the online journal.)

of an imperfect PSF generated from unresolved sources in the field.

The secondary unresolved component is  $1''.0$  (4.9 kpc in projection) offset from the Sérsic center. This component does not show obvious variability. It is too bright ( $M_r = -19.4$ ) to be a star cluster inside the host galaxy or a satellite dwarf elliptical galaxy, although it could be a second merging, compact galaxy. It is not likely to be a stellar object unless it is a foreground star along the line of sight. The position angle to the primary compact object is  $49^\circ$ , or  $\sim 30^\circ$  with respect to the secondary radio jet, making it unlikely to be a bright spot associated with an optical jet of the central AGN. A better understanding of this component will require sensitive, higher-resolution imaging.

The brightest visual companion at slightly greater distance ( $r > 4''$ ;  $\sim 20$  kpc) has  $m_r = 21.6$  (AB mag), which corresponds to  $\sim 6 \times 10^9 L_\odot$  in the  $r'$ -band after  $k$ -corrections assuming the redshift of W2332–5056. There are no obvious disturbed morphological features brighter than  $1/5$  of the luminosity of W2332–5056 to suggest that the host galaxy is an early/intermediate-stage major merger system.

### 3.6. SED Modeling

We model the broadband SED of W2332–5056 from the ultraviolet (UV) to the mid-IR with a combination of host galaxy and AGN components using the empirical SED templates of Assef et al. (2010). One challenge is that the source is clearly variable at optical wavelengths (see Section 3.4 and Figure 6). Indeed, the red optical SED observed by Magellan in 2008 is difficult to reconcile with the very blue  $z' - J$  color implied by the 2MASS  $J$ -band photometry obtained in 1999 unless we invoke variability. We therefore divide the photometric data into three epochs (1991.7–1992.9, 1999.9, and 2008.9–2010.5, in roughly 3 yr time bins) for SED fitting purposes (Figure 8).

The multi-epoch SED fitting was done requiring a common, non-variable host galaxy using a combination of empirical starburst, disk galaxy, and elliptical galaxy templates from Assef et al. (2010) to represent the different age stellar populations in W2332–5056. We required these SED galaxy components to match the morphological modeling discussed in Section 3.5; namely, we required that the  $r'$  fluxes from the three galaxy components sum to one third of the total  $r'$  flux, or  $\sim 60 \mu\text{Jy}$ . For the AGN component, we adopted a modified AGN SED template in which the warm dust emission at  $\lambda > 1 \mu\text{m}$  is replaced by power-law emission to continue the accretion disk emission to longer wavelengths. This modification was made in order to satisfy a reasonable fit between the  $r'$ -band and W2. We also apply foreground dust extinction toward the AGN to accommodate the red optical color. This modified obscured AGN component is reminiscent of the synchrotron emission that characterizes blazars at these wavelengths (Abdo et al. 2010); the WISE colors of W2332–5056 put it close to the blazar strip of Massaro et al. (2012). Blazars, conventionally considered to be the radio galaxies with relativistic jets close to the line of sight, exhibit large amplitude luminosity variations over hours to days (see the review by Ulrich et al. 1997). However, the interpretation of W2332–5056 as a blazar is inconsistent with the radio morphology, nor do we see strong evidence for short-time scale variability at optical and mid-IR wavelengths. We do not address this blazar interpretation further here.

The results of the model fitting are presented in Figure 8. The GALEX observations, obtained between 2003 and 2005, would appear to present a challenge. On the one hand, they could be associated with a variable AGN component observed during an epoch when we do not have other photometry available to use in the SED modeling. On the other hand, they could be associated with the non-variable host galaxy or a combination of the host and variable AGN. In practice, our results do not depend strongly on the GALEX data. If we completely ignore those UV data, our best-fit model implies a heavily obscured AGN during the latest epoch with  $E(B - V) = 0.81 \pm 0.05$ . For this model, the host galaxy, dominated by the starburst (e.g., irregular galaxy) component, goes through the GALEX photometric points with the best-fit luminosity to the irregular component being  $L_{\text{im}} = (2.6 \pm 1.5) \times 10^{10} L_\odot$ . Additionally, the  $\chi^2_{\text{red}}$  increases from 1.65 (dof = 6) to 3.26 (dof = 7) if we exclude the irregular component in the SED fitting. These suggest that the GALEX photometry corresponds to the host galaxy with little AGN contribution. If we redo the fitting under that assumption, the resulting AGN obscuration basically remains the same,  $E(B - V) = 0.82 \pm 0.04$ , and the starburst component luminosity becomes slightly more robust, but is essentially unchanged:  $L_{\text{im}} = (3.2 \pm 1.0) \times 10^{10} L_\odot$ . It is this latter case where we assume that the decade-old GALEX photometry is due to the host galaxy, which we show in Figure 8.

An obscured AGN dominates the optical and WISE photometry for the most recent epoch, while 10 yr ago, when the 2MASS photometry was obtained, our modeling is based on fewer bands but suggests a slightly less luminous AGN with a similar level of obscuration,  $E(B - V) = 0.8$ . The AGN reddening in these epochs is slightly higher than the  $E(B - V) = 0.4 \pm 0.1$  implied from the X-ray column,  $N_{\text{H}} \sim 2.3 \pm 0.5 \times 10^{21} \text{ cm}^{-2}$  (Section 3.3), if the conventional Milky Way value of  $N_{\text{H}}/E(B - V) \sim 5.9 \times 10^{21} \text{ cm}^{-2}$  (Bohlin et al. 1978; Rachford et al. 2002) applies. Finally, the same fitting was applied to the Digitized Sky Survey (DSS) photometry for the epoch 1991.7–1992.9. Remarkably, the best-fit model

shows that no AGN emission component is necessary and is relatively well modeled by the host galaxy component alone. The DSS *B*-band, taken in 1975, is not included in the fitting due to its early observational epoch, but appears not to affect the fitting results if included. The best-fit AGN amplitude is nominally zero, suggesting that only  $\sim 20$  yr in the past W2332–5056 did not have appreciable nuclear activity. We note that, although the best-fit model has relatively larger uncertainty due to the quality of the DSS photometry, the strong variation in the optical band over two decades is significant. The interpolation of our high-quality optical photometry measurements in the current epoch (2008–2010) suggests a flux of  $\sim 300 \mu\text{Jy}$  in the DSS *I*-band measurement,  $>10\sigma$  higher than the measurement of  $80 \pm 20 \mu\text{Jy}$  in the 1991–1992 epoch.

### 3.7. Host Galaxy—A PRONGS Candidate

FR-II radio sources are almost invariably found to be associated with large elliptical galaxies (Matthews et al. 1964; Owen & Laing 1989). Such hosts typically have de Vaucouleurs'  $r^{1/4}$  profiles (Owen & White 1991), corresponding to a Sérsic index of 4. However, a class of radio sources hosted in star-forming galaxies has been identified by Norris et al. (2006) and later named Powerful Radio Objects Nested in Galaxies with Star Formation (PRONGS; Mao et al. 2010; Norris et al. 2012). These objects are radio-loud AGNs ( $\gtrsim 10^{24} \text{ W Hz}^{-1}$ ) with radio lobes  $<200$  kpc that are hosted by spiral or starburst galaxies. Mao et al. (2010) discovered 50 PRONGS in a systematic search of a  $7 \text{ deg}^2$  field in the Australia Telescope Large Area Survey (Norris et al. 2006; Middelberg et al. 2008). Prior to this work, two radio-loud, edge-on disk galaxies (NGC 612 and 0313-192) were known in the local universe (Ekers et al. 1978; Ledlow et al. 2001; Keel et al. 2006; Emonts et al. 2008). NGC 612 has a collimated FR-I-like jet and an FR-II-like lobe with a bright hot spot on the other end, sometimes described as a hybrid-morphology radio source (HYMORS; Gopal-Krishna & Wiita 2000), while 0313-192 has a typical FR-I morphology. There are a few other similar nearby examples where radio-loud objects are hosted in disk-like galaxies such as 3C305 (Heckman et al. 1982), 3C293 (van Breugel et al. 1984), B2 0722+30 (Emonts et al. 2009), PKS 1814-636 (Morganti et al. 2011), and SDSS J1409–0302 (Hota et al. 2011). They could be associated with PRONGS but perhaps at a slightly different evolutionary phase. Previous work has suggested that PRONGS may represent an early evolutionary stage for radio-loud galaxies. An example is given by Norris et al. (2012), who present a very long baseline interferometry (VLBI) image of a highly embedded, compact core–jet AGN with 1.7 kpc long jets in IRAS F00183-7111, a ULIRG with  $L_{\text{bol}} \sim 9 \times 10^{12} L_{\odot}$  and substantial star formation activity.

The optical morphology (Section 3.5) suggests that the host galaxy of W2332–5056 has a modest disk (Sérsic index  $\sim 0.9$ ), not much bigger than the Milky Way in size and luminosity. With a 5 GHz to 4400 Å continuum flux density ratio  $\gg 10$ , the W2332–5056 system is clearly hosting a radio-loud AGN according to the definition of Kellermann et al. (1989). Although it hosts a HYMORS-like source, the galaxy of the W2332–5056 system seems to be a normal disk galaxy, making it a candidate for the rare PRONGS classification.

Based on its rest-frame near-UV luminosity  $\nu L_{\nu} \sim 1.1 \times 10^{10} L_{\odot}$  from the host galaxy SED, we estimate a star formation rate of  $5 M_{\odot} \text{ yr}^{-1}$  in W2332–5056, using Equation (1) of Kennicutt (1998) with no significant dust attenuation assumed. The total luminosity of W2332–5056 up to  $22 \mu\text{m}$  is  $3.7 \times 10^{11} L_{\odot}$ . The non-detection by *AKARI*, *IRAS*, and the SPT

limit the far-IR (FIR) luminosity ( $L_{\text{FIR}}$ ) to  $3.5 \times 10^{12} L_{\odot}$  if an Arp 220-like FIR SED is assumed. However, this Arp 220-like SED model does not match the observed optical-to-near-IR photometry of the system. If a fraction of the star formation activity is highly obscured at optical wavelengths ( $A_V > 40$ ) but releasing energy via dust emission, the  $22 \mu\text{m}$  (W4) flux density limits  $L_{\text{FIR}}$  to  $< 3.5 \times 10^{11} L_{\odot}$  or  $< 30 M_{\odot} \text{ yr}^{-1}$  (i.e., 10% that of Arp 220; Anantharamaiah et al. 2000). Thus, the host galaxy of W2332–5056 is not likely to be undergoing a major starburst. This star formation rate is close to a typical quiescent disk galaxy, unlike the hosts of other PRONGS.

## 4. DISCUSSION

Observationally, as discussed in Section 3, W2332–5056 shows (1) an unusual, complex radio morphology, including curved jets, and an emission complex within the central 25 kpc, (2) a disk-like galaxy as the host of an FR-I/FR-II hybrid radio source, (3) long-term (3–20 yr) optical–near-IR nuclear variability, and (4) a DPE profile in H $\beta$  and H $\alpha$ . The standard interpretation of DPEs in which the BLs originate from the surface of a geometrically thin accretion disk around a single central SMBH is not ruled out by the observed optical spectrum and does not prohibit the observed photometric variability. Our best-fit single AGN model (Section 3.2.2) entails an inclined elliptical ( $e = 0.6$ ) thin disk at a viewing angle of  $\sim 42^\circ$  from face-on. The lifetime of high eccentricity could be a concern, although the circularization of the disk is from the inside-out; thus, the outer disk can retain its ellipticity for longer periods of time (Syer & Clarke 1992). On the other hand, a warped disk or a single-arm spiral disk can mimic the BL profile similar to that from an elliptical thin disk. These possibilities can be examined through the BL profile variability from long-term spectroscopic monitoring and detailed line profile modeling, although there is no detectable variation in the line profile over the  $\sim 6$  month period separating the two GMOS observations.

The radio emission features, however, indicate that W2332–5056 has a more complicated configuration than a typical disk emitter. First, the viewing angles of the primary jets and the accretion disk in the thin disk model are not consistent with each other. The flux ratio of the two primary radio jets along the inner  $4''.5$ – $9''.5$  is  $\sim 2$ . This fairly small ratio suggests that the primary jets are close to being in the face-on plane (an angle between the jet flow direction and the line of sight  $> 80^\circ$ ) unless the two jets are intrinsically different. The inclination of the best-fit elliptical disk, however, is  $30^\circ$ – $50^\circ$  after relaxing other fitting parameters, such as eccentricity to  $e = 0.2$ – $0.8$ . Second, the appearance of the radio emission complex (such as components “D” and “F” in Figure 3) within 25 kpc (projected) from the core suggests some event or continuous activities within the past 70,000 yr if the complex originated from the core and propagates relativistically. Since the complex has a high radio luminosity ( $\sim 10^{40} \text{ erg s}^{-1}$ ) and does not have optical or mid-IR counterparts, the assumption that it originates from the AGN is viable. The causes of the radio complex could easily create imprints (such as a hot spot or a gap) in the geometric configuration of the thin disk, if the disk configuration is not part of the cause itself.

We should note that if a rotating BH is misaligned with the accretion disk, the material will be realigned due to Lense-Thirring drag (Bardeen & Petterson 1975). SMBH–accretion disk realignment, which is sometimes attributed to the cause of the XRGs (see Section 1), has a timescale

shorter than Myr for a SMBH of  $10^8 M_\odot$  under typical AGN accretion rates (Dennett-Thorpe et al. 2002). We crudely estimate the SMBH mass of W2332–5056 (with a radio luminosity  $\nu L_\nu = 5.7 \times 10^{40} \text{ erg s}^{-1}$  at 5.6 GHz and a core X-ray luminosity  $L(2\text{--}10 \text{ keV}) = 4.1 \times 10^{44} \text{ erg s}^{-1}$ ) to be  $\sim 4 \times 10^8 M_\odot$  using the fundamental plane of BH accretion (Merloni et al. 2003; Gültekin et al. 2009). The uncertainty on this mass is a factor of  $\sim 8$  due to the scatter in the empirical relations among X-ray luminosity, radio luminosity, and BH mass. The large uncertainty in the SMBH mass will not affect the realignment timescale too much since it has a low dependency ( $\propto M^{-1/16}$ ) on the BH mass. It is worth considering that the radio complex is the result of jet reorientation due to the BH–disk realignment in the past 0.1 Myr, although the cause of the initial misalignment between the SMBH spin and the accretion disk is unknown. Under this scenario, the double-peaked BL profile is produced by the warped disk induced in the realignment process and the two curved radio jets W2332–5056 are the relics of the early realignment stage.

The other plausible scenario involves two SMBHs residing in the disk-like host of W2332–5056 as a result of a major galaxy–galaxy merger. Based on numerical simulations, disk formation takes  $\sim 1\text{--}2$  Gyr after the close encounter of the major merging event of the parent gas-rich galaxy pair (Robertson et al. 2006). This period of time is long enough for two SMBHs to sink down to the center of the merged system (Begelman et al. 1980) and reach the stalling separation at a distance of order pc or less. In this case, double-peaked Balmer lines arise from a long-lived eccentricity or single-arm spiral disk induced by the dynamical interaction with the second SMBH within a misaligned orbital plane, as discussed by Eracleous et al. (1995) and Bogdanović et al. (2008). The binary interaction could be responsible for disk warping or a precession of the plane of the disk, as indicated by the mismatched inclination angles of the disk between now (implied by the spectroscopic models) and a few hundred thousand years ago (implied by the close-to-equal brightnesses of the primary jets on the two sides) and leaves the curved radio jets (i.e., jet precession; Roos 1988), as well as the enigmatic radio features.

This scenario might apply not only in W2332–5056, but also in some DPEs. A recent VLBI survey of SDSS DPEs with FIRST detections shows that two out of six studied DPEs have compact radio cores at kiloparsec scale separations (R. Deane, in preparation). The radio galaxy 4C37.11 contains a SMBH binary system with a 7.3 pc separation and  $\sim 1.5 \times 10^8 M_\odot$  in mass (Rodriguez et al. 2006). In addition, there are several radio-bright DPEs in which double nuclei with separations of a few kpc are seen in high-resolution radio mapping, such as SDSS J1536+0441 (Wrobel & Laor 2009; Bondi & Pérez-Torres 2010), SDSS J1502+1115 (Fu et al. 2011b), and SDSS J1425+3231 (Frey et al. 2012). These results indicate that some DPE systems indeed host dual AGNs.

The current resolution limits of radio and millimeter interferometers, such as VLBI networks and ALMA, reach  $\sim 5$  mas (Middelberg & Bach 2008; Wootten & Thompson 2009). At this resolution, compact radio/mm sources with projected distances  $> 25$  pc at  $z = 0.3447$  can be resolved. Although this high-contrast aperture synthesis imaging can recover high surface brightness structures such as highly collimated jets near their launch point, 25 pc physical resolution cannot resolve a SMBH binary at an “intermediate” merging stage with stalling separations of 0.01–1 pc (Begelman et al. 1980; Yu 2002). Current resolutions can, however, study an early-stage SMBH

merger, when the scattering of circumnuclear stars is the dominant process for losing angular momentum.

## 5. SUMMARY

We report the discovery of W2332–5056, a radio galaxy at  $z = 0.3447$  with an extraordinary radio morphology and optical spectroscopic features. We summarize the observational facts as follows.

1. The galaxy exhibits hybrid features between FR-I and FR-II morphology and the radio continuum map shows a winding Doppler-boosted FR-II jet, a pair of curved jets, a bright core, and complex emission within 25 kpc.
2. The host galaxy of W2332–5056, unlike the elliptical hosts of most FR-II objects, is disk-like.
3. We see long-term (3–20 yr) optical-near-IR brightness variations from the AGN component.
4. The optical spectrum of W2332–5056 shows offsets of  $\sim 3800 \text{ km s}^{-1}$  between the centroids of the BL and NL components of H $\alpha$  and H $\beta$ .

We consider the following two scenarios to explain these unusual properties.

1. W2332–5056 has a single spinning SMBH misaligned with its accretion disk. The realignment of the accretion disk due to dynamical drag produces the broadband Balmer profiles, leaving reorientated jets in the process and creating the complicated radio morphology. The cause of the initial misalignment is unknown.
2. W2332–5056 has a SMBH binary with a separation on the order of pc. The dynamical interaction between the two SMBHs induces the warping or spiral pattern in the disk of one SMBH, which generates the BL profile. The curved jets and radio complex within the central 25 kpc reflect some perturbation from the second SMBH on the accretion disk.

Our results and analysis can neither rule out nor confirm either of these two scenarios. The real nature of W2332–5056 remains a mystery. Further investigations will be required to resolve the complicated structures within a 5'' radius of the core, confirm their nature, and even probe the sub-components in the core, if there are any. We are currently pursuing high-resolution radio mapping of W2332–5056 to investigate our hypotheses of the radio morphology formation and also monitor the galaxy’s optical spectrum and photometry. If our hypothesis is confirmed, W2332–5056 will be an exciting system in which to study the physics of a SMBH merger event.

The authors thank the anonymous referee for the constructive comments and inspiring suggestions throughout the whole paper. We acknowledge Joaquin Vieira for verifying the W2332–5056 non-detection in the SPT survey map. We thank Roger Deane for sharing his VLBI work prior to the publication. We also appreciate the comments and suggestions by Colin Lonsdale and the discussions with Michael Eracleous and Laura Blecha in the “Binary Black Holes and Dual AGN” meeting in Tucson in 2012. R.J.A. was supported in part by Gemini-CONICYT grant number 32120009. R.J.A. was also supported in part by an appointment to the NASA Postdoctoral Program at the Jet Propulsion Laboratory, administered by Oak Ridge Associated Universities through a contract with NASA. This publication makes use of data products from WISE, which is a joint project of the University of California, Los

Angeles and the Jet Propulsion Laboratory, California Institute of Technology, funded by the National Aeronautics and Space Administration. Based on observations obtained at the Gemini Observatory, which is operated by the Association of Universities for Research in Astronomy, Inc., under a cooperative agreement with the NSF on behalf of the Gemini partnership: the National Science Foundation (United States), the Science and Technology Facilities Council (United Kingdom), the National Research Council (Canada), CONICYT (Chile), the Australian Research Council (Australia), Ministério da Ciencia, Tecnologia e Inovao (Brazil) and Ministerio de Ciencia, Tecnologa e Innovacin Productiva (Argentina). The Australia Telescope is funded by the Commonwealth of Australia for operation as a National Facility managed by CSIRO. This research has made use of the NASA/IPAC Extra-galactic Database (NED), which is operated by the Jet Propulsion Laboratory, California Institute of Technology, under contract with the National Aeronautics and Space Administration. This research has made use of the NASA/IPAC Infrared Science Archive, which is operated by the Jet Propulsion Laboratory, California Institute of Technology, under contract with the National Aeronautics and Space Administration.

**Facilities:** ATCA (CABB), WISE, Spitzer (IRAC), SOAR (SOI imager), Gemini:South (GMOS spectrograph), CXO (ACIS-I)

## REFERENCES

- Abdo, A. A., Ackermann, M., Agudo, I., et al. 2010, *ApJ*, **716**, 30
- Alexander, D. M., & Hickox, R. C. 2012, *NewA*, **56**, 93
- Anantharamaiah, K. R., Viallefond, F., Mohan, N. R., Goss, W. M., & Zhao, J. H. 2000, *ApJ*, **537**, 613
- Andersson, K., Benson, B. A., Ade, P. A. R., et al. 2011, *ApJ*, **738**, 48
- Assef, R. J., Kochanek, C. S., Brodwin, M., et al. 2010, *ApJ*, **713**, 970
- Bardeen, J. M., & Petterson, J. A. 1975, *ApJL*, **195**, L65
- Barrows, R. S., Lacy, C. H. S., Kennefick, D., Kennefick, J., & Seigar, M. S. 2011, *NewA*, **16**, 122
- Barrows, R. S., Stern, D., Madsen, K., et al. 2012, *ApJ*, **744**, 7
- Baumgartner, T. W., & Shapiro, S. L. 2011, *PhT*, **64**, 32
- Begelman, M. C., Blandford, R. D., & Rees, M. J. 1980, *Natur*, **287**, 307
- Bogdanović, T., Smith, B. D., Sigurdsson, S., & Eracleous, M. 2008, *ApJS*, **174**, 455
- Bohlin, R. C., Savage, B. D., & Drake, J. F. 1978, *ApJ*, **224**, 132
- Bondi, M., & Pérez-Torres, M.-A. 2010, *ApJL*, **714**, L271
- Bonning, E. W., Shields, G. A., & Salviander, S. 2007, *ApJL*, **666**, L13
- Boroson, T. A., & Lauer, T. R. 2009, *Natur*, **458**, 53
- Campanelli, M., Lousto, C., Zlochower, Y., & Merritt, D. 2007, *ApJL*, **659**, L5
- Cannizzo, J. K., Lee, H. M., & Goodman, J. 1990, *ApJ*, **351**, 38
- Capetti, A., Zamfir, S., Rossi, P., et al. 2002, *A&A*, **394**, 39
- Chen, K., & Halpern, J. P. 1989, *ApJ*, **344**, 115
- Cheung, C. C., Healey, S. E., Landt, H., Verdoes Kleijn, G., & Jordán, A. 2009, *ApJS*, **181**, 548
- Civano, F., Elvis, M., Lanzuisi, G., et al. 2010, *ApJ*, **717**, 209
- Collin-Souffrin, S., & Dumont, A. M. 1989, *A&A*, **213**, 29
- Comerford, J. M., Gerke, B. F., Stern, D., et al. 2012, *ApJ*, **753**, 42
- Cutri, R. M., Wright, E. L., Conrow, T., et al. 2012, Explanatory Supplement to the WISE All-Sky Data Release Products, 1
- Dennett-Thorpe, J., Scheuer, P. A. G., Laing, R. A., et al. 2002, *MNRAS*, **330**, 609
- Dotti, M., Colpi, M., Haardt, F., & Mayer, L. 2007, *MNRAS*, **379**, 956
- Dotti, M., Ruszkowski, M., Paredi, L., et al. 2009, *MNRAS*, **396**, 1640
- Dumont, A. M., & Collin-Souffrin, S. 1990a, *A&A*, **229**, 313
- Dressler, A., Bigelow, B., Hare, T., et al. 2011, *PASP*, **123**, 288
- Dumont, A. M., & Collin-Souffrin, S. 1990b, *A&AS*, **83**, 71
- Ekers, R. D., Goss, W. M., Kotanyi, C. G., & Skellern, D. J. 1978, *A&A*, **69**, L21
- Emonts, B. H. C., Morganti, R., Oosterloo, T. A., et al. 2008, *MNRAS*, **387**, 197
- Emonts, B. H. C., Tadhunter, C. N., Morganti, R., et al. 2009, *MNRAS*, **396**, 1522
- Eracleous, M., Boroson, T. A., Halpern, J. P., & Liu, J. 2012, *ApJS*, **201**, 23
- Eracleous, M., & Halpern, J. P. 2003, *ApJ*, **599**, 886
- Eracleous, M., Lewis, K. T., & Flohic, H. M. L. G. 2009, *NewAR*, **53**, 133
- Eracleous, M., Livio, M., Halpern, J. P., & Storchi-Bergmann, T. 1995, *ApJ*, **438**, 610
- Escala, A., Larson, R. B., Coppi, P. S., & Mardones, D. 2004, *ApJ*, **607**, 765
- Escala, A., Larson, R. B., Coppi, P. S., & Mardones, D. 2005, *ApJ*, **630**, 152
- Fanaroff, B. L., & Riley, J. M. 1974, *MNRAS*, **167**, 31P
- Frey, S., Paragi, Z., An, T., & Gabányi, K. É. 2012, *MNRAS*, **425**, 1185
- Fu, H., Myers, A. D., Djorgovski, S. G., & Yan, L. 2011a, *ApJ*, **733**, 103
- Fu, H., Yan, L., Myers, A. D., et al. 2012, *ApJ*, **745**, 67
- Fu, H., Zhang, Z.-Y., Assef, R. J., et al. 2011b, *ApJL*, **740**, L44
- Gezari, S., Halpern, J. P., & Eracleous, M. 2007, *ApJS*, **169**, 167
- González, J. A., Hannam, M., Sperhake, U., Brügmann, B., & Husa, S. 2007, *PhRvL*, **98**, 231101
- Gopal-Krishna, Biermann, P. L., Gergely, L. Á., & Wiita, P. J. 2010, *RAA*, **12**, 127
- Gopal-Krishna, Biermann, P. L., & Wiita, P. J. 2003, *ApJL*, **594**, L103
- Gopal-Krishna, & Wiita, P. J. 2000, *A&A*, **363**, 507
- Green, P. J., Myers, A. D., Barkhouse, W. A., et al. 2010, *ApJ*, **710**, 1578
- Gregory, P. C., Vavasour, J. D., Scott, W. K., & Condon, J. J. 1994, *ApJS*, **90**, 173
- Gültekin, K., Cackett, E. M., Miller, J. M., et al. 2009, *ApJ*, **706**, 404
- Hambly, N. C., Irwin, M. J., & MacGillivray, H. T. 2001, *MNRAS*, **326**, 1295
- Healy, J., Herrmann, F., Hinder, I., et al. 2009, *PhRvL*, **102**, 041101
- Heckert, T. M., Miley, G. K., Balick, B., van Breugel, W. J. M., & Butcher, H. R. 1982, *ApJ*, **262**, 529
- High, F. W., Stalder, B., Song, J., et al. 2010, *ApJ*, **723**, 1736
- Hodges-Kluck, E. J., Reynolds, C. S., Cheung, C. C., & Miller, M. C. 2010, *ApJ*, **710**, 1205
- Hook, I. M., Jørgensen, I., Allington-Smith, J. R., et al. 2004, *PASP*, **116**, 425
- Hota, A., Sirothia, S. K., Ohyama, Y., et al. 2011, *MNRAS*, **417**, L36
- Iguchi, S., Okuda, T., & Sudou, H. 2010, *ApJL*, **724**, L166
- Jarrett, T. H., Cohen, M., Masci, F., et al. 2011, *ApJ*, **735**, 112
- Jenet, F. A., Lommen, A., Larson, S. L., & Wen, L. 2004, *ApJ*, **606**, 799
- Ju, W., Greene, J. E., Rafikov, R. R., Bickerton, S. J., & Badenes, C. 2013, *ApJ*, **777**, 44
- Keel, W. C., White, R. E., III, Owen, F. N., & Ledlow, M. J. 2006, *AJ*, **132**, 2233
- Kellermann, K. I., Sramek, R., Schmidt, M., Shaffer, D. B., & Green, R. 1989, *AJ*, **98**, 1195
- Kennicutt, R. C., Jr. 1998, *ARA&A*, **36**, 189
- Komossa, S. 2012, *AdAst*, **2012**, 364973
- Komossa, S., Burwitz, V., Hasinger, G., et al. 2003, *ApJL*, **582**, L15
- Landt, H., Cheung, C. C., & Healey, S. E. 2010, *MNRAS*, **408**, 1103
- Leahy, J. P., & Parma, P. 1992, in Proc. 7th IAP Meeting on Extragalactic Radio Sources—From Beams to Jets, ed. J. Roland, H. Sol, & G. Pelletier (Cambridge: Cambridge Univ. Press), 307
- Leahy, J. P., & Williams, A. G. 1984, *MNRAS*, **210**, 929
- Ledlow, M. J., Owen, F. N., Yun, M. S., & Hill, J. M. 2001, *ApJ*, **552**, 120
- Lewis, K. T., Eracleous, M., & Storchi-Bergmann, T. 2010, *ApJS*, **187**, 416
- Maloney, P. R., Begelman, M. C., & Pringle, J. E. 1996, *ApJ*, **472**, 582
- Mao, M. Y., Norris, R. P., Sharp, R., & Lovell, J. E. J. 2010, in IAU Symp. 267, Co-Evolution of Central Black Holes and Galaxies, ed. B. Peterson, R. Somerville, & T. Storchi-Bergmann (Cambridge: Cambridge Univ. Press), 119
- Massaro, F., D'Abrusco, R., Tosti, G., et al. 2012, *ApJ*, **750**, 138
- Matthews, T. A., Morgan, W. W., & Schmidt, M. 1964, *ApJ*, **140**, 35
- Mauch, T., Murphy, T., Buttery, H. J., et al. 2003, *MNRAS*, **342**, 1117
- McConnell, N. J., Ma, C.-P., Gebhardt, K., et al. 2011, *Natur*, **480**, 215
- McConnell, N. J., Ma, C.-P., Murphy, J. D., et al. 2012, *ApJ*, **756**, 179
- Meier, D. L., Koide, S., & Uchida, Y. 2001, *Sci*, **291**, 84
- Merloni, A., Heinz, S., & di Matteo, T. 2003, *MNRAS*, **345**, 1057
- Merritt, D., & Ekers, R. D. 2002, *Sci*, **297**, 1310
- Merritt, D., & Milosavljević, M. 2005, *LRR*, **8**, 8
- Middelberg, E., & Bach, U. 2008, *RPPh*, **71**, 066901
- Middleberg, E., Norris, R. P., Cornwell, T. J., et al. 2008, *AJ*, **135**, 1276
- Morganti, R., Holt, J., Tadhunter, C., et al. 2011, *A&A*, **535**, A97
- Norris, R. P., Afonso, J., Appleton, P. N., et al. 2006, *AJ*, **132**, 2409
- Norris, R. P., Lenc, E., Roy, A. L., & Spoon, H. 2012, *MNRAS*, **422**, 1453
- Ogilvie, G. I. 2001, *MNRAS*, **325**, 231
- Owen, F. N., O'Dea, C. P., Inoue, M., & Eilek, J. A. 1985, *ApJL*, **294**, L85
- Owen, F. N., & Laing, R. A. 1989, *MNRAS*, **238**, 357
- Owen, F. N., & White, R. A. 1991, *MNRAS*, **249**, 164
- Peng, C. Y., Ho, L. C., Impey, C. D., & Rix, H.-W. 2002, *AJ*, **124**, 266
- Peng, C. Y., Ho, L. C., Impey, C. D., & Rix, H.-W. 2010, *AJ*, **139**, 2097
- Popović, L. Č. 2012, *NewAR*, **56**, 74
- Rachford, B. L., Snow, T. P., Tumlinson, J., et al. 2002, *ApJ*, **577**, 221

- Rees, M. J. 1988, *Natur*, **333**, 523
- Robertson, B., Bullock, J. S., Cox, T. J., et al. 2006, *ApJ*, **645**, 986
- Rodriguez, C., Taylor, G. B., Zavala, R. T., et al. 2006, *ApJ*, **646**, 49
- Roos, N. 1988, *ApJ*, **334**, 95
- Saripalli, L., & Subrahmanyam, R. 2009, *ApJ*, **695**, 156
- Shen, Y., Liu, X., Loeb, A., & Tremaine, S. 2013, *ApJ*, **775**, 49
- Shields, G. A., Bonning, E. W., & Salvander, S. 2009, *ApJ*, **696**, 1367
- Shields, G. A., Rosario, D. J., Smith, K. L., et al. 2009, *ApJ*, **707**, 936
- Skrutskie, M. F., Cutri, R. M., Stiening, R., et al. 2006, *AJ*, **131**, 1163
- Steinhardt, C. L., Schramm, M., Silverman, J. D., et al. 2012, *ApJ*, **759**, 24
- Stern, D., Assef, R. J., Benford, D. J., et al. 2012, *ApJ*, **753**, 30
- Stern, D., Tozzi, P., Stanford, S. A., et al. 2002, *AJ*, **123**, 2223
- Storchi-Bergmann, T., Nemmen da Silva, R., Eracleous, M., et al. 2003, *ApJ*, **598**, 956
- Sudou, H., Iguchi, S., Murata, Y., & Taniguchi, Y. 2003, *Sci*, **300**, 1263
- Syer, D., & Clarke, C. J. 1992, *MNRAS*, **255**, 92
- Tang, S., & Grindlay, J. 2009, *ApJ*, **704**, 1189
- Tsalmantza, P., Decarli, R., Dotti, M., & Hogg, D. W. 2011, *ApJ*, **738**, 20
- Ulrich, M.-H., Maraschi, L., & Urry, C. M. 1997, *ARA&A*, **35**, 445
- van Breugel, W., Heckman, T., Butcher, H., & Miley, G. 1984, *ApJ*, **277**, 82
- Vanderlinde, K., Crawford, T. M., de Haan, T., et al. 2010, *ApJ*, **722**, 1180
- Walker, A. R., Bocca, M., Bonati, M., et al. 2003, *Proc. SPIE*, **4841**, 286
- Wootten, A., & Thompson, A. R. 2009, *IEEEEP*, **97**, 1463
- Worrall, D. M., Birkinshaw, M., & Cameron, R. A. 1995, *ApJ*, **449**, 93
- Wright, A. E., Griffith, M. R., Burke, B. F., & Ekers, R. D. 1994, *ApJS*, **91**, 111
- Wright, E. L., Eisenhardt, P. R. M., Mainzer, A. K., et al. 2010, *AJ*, **140**, 1868
- Wrobel, J. M., & Laor, A. 2009, *ApJL*, **699**, L22
- Wu, S.-M., Wang, T.-G., & Dong, X.-B. 2008, *MNRAS*, **389**, 213
- Yokosawa, M., & Inoue, M. 1985, *PASJ*, **37**, 655
- Yu, Q. 2002, *MNRAS*, **331**, 935